Aging Cell

WILEY

RESEARCH ARTICLE OPEN ACCESS

Translational Remodeling of the Synaptic Proteome During Aging

Cinzia Caterino[1] | Martino Ugolini[2,3] | William Durso[1] | Kristina Jevdokimenko[4] | Marco Groth[1] | Konstantin Riege[1] | Matthias Görlach[1,†] | Eugenio Fornasiero[4,5] | Alessandro Ori[1] | Steve Hoffmann[1] | Alessandro Cellerino[1,6]

[1]Leibniz Institute on Aging—Fritz Lipmann Institute e.V. (FLI), Jena, Germany | [2]Center for Integrative Genomics (CIG), University of Lausanne (UNIL), Lausanne, Switzerland | [3]Max Planck Institute of Molecular Cell Biology and Genetics (MPI-CBG), Dresden, Germany | [4]Institute of Neuro- and Sensory Physiology, University Medical Center Göttingen, Göttingen, Germany | [5]Department of Life Sciences, University of Trieste, Trieste, Italy | [6]Scuola Normale Superiore, BioSNS, c/o Istituto di Biofisica del CNR, Pisa, Italy

Correspondence: Alessandro Cellerino (alessandro.cellerino@sns.it)

Received: 4 December 2024 | **Revised:** 16 September 2025 | **Accepted:** 1 October 2025

Funding: The authors received no specific funding for this work.

Keywords: aging | alternative splicing | bioinformatics | RNA-Seq | synaptosomes

ABSTRACT

An important hallmark of aging is the loss of proteostasis, which can lead to the formation of protein aggregates and mitochondrial dysfunction in neurons. Although it is well known that protein synthesis is finely regulated in the brain, especially at synapses, where mRNAs are locally translated in an activity-dependent manner, little is known as to the changes in the synaptic proteome and transcriptome during aging. Therefore, this work aims to elucidate the relationship between the transcriptome and proteome at the soma and synaptic levels during aging. Proteomic and transcriptomic data analysis reveal that, in young animals, proteins and transcripts are correlated and synaptic regulation is driven by changes in the soma. During aging, there is a decoupling between transcripts and proteins and between somatic and synaptic compartments. Furthermore, the soma-synapse gradient of ribosomal genes changes upon aging, that is, ribosomal transcripts are less abundant and ribosomal proteins are more abundant in the synaptic compartment of old mice with respect to younglings. Additionally, transcriptomics data highlight a difference in the splicing of certain synaptic mRNA with aging. Taken together, our data provide a valuable resource for the study of the aging synapse.

1 | Introduction

Brain aging is characterized by a progressive reduction of cortical gray matter volume (Fjell et al. 2009; Lemaître et al. 2005, 2012; Raz et al. 2005). Surprisingly, cortical shrinkage is not correlated with significant neuronal death during normal brain aging but represents a pathological feature associated with neurodegenerative diseases (Morrison and Hof 2007; Pakkenberg et al. 2003). Cortical shrinkage must then be mainly the result of changes in the network of neuronal connections (neuropil), and indeed aged pyramidal cortical neurons are affected by a reduction of synaptic spines (Dickstein et al. 2007, 2013) and imbalances in neurotransmitter signaling (Leventhal et al. 2003; Wang et al. 2011). These synaptic changes are likely the cause of age-dependent deficits in functions such as perceptual speed and working memory (Buckner 2004; Nyberg et al. 2012).

Neurons are cells of a peculiar morphology that comprise complex and extensive neurites. Neurites can have a length that is orders of magnitude larger than the soma diameter and most of

Cinzia Caterino and Martino Ugolini contributed equally to this study.

[†]Deceased.

the neuronal cytoplasm is contained in neurites. Dispatching somatically synthesized proteins to distant compartments is a demanding process and it has become increasingly clear that many transcripts coding for synaptic proteins are transported to distant sites (von Kügelgen and Chekulaeva 2020 and references therein) and that most of the neuritic proteome is synthesized locally (Zappulo et al. 2017). Local synaptic translation is indispensable both for synapse maintenance and for activity-dependent synaptic plasticity both during development and in adulthood (Cioni et al. 2018; Glock et al. 2017; Holt and Schuman 2013; Holt et al. 2019; Sun et al. 2021). Transcripts coding for synaptic proteins are subject to alternative splicing and are enriched in specific motifs that support local translation. Neuronal aging is known to affect splicing at a global level and altered splicing is a likely driving factor of Alzheimer's disease (Raj et al. 2018).

Although synaptic translation has been extensively analyzed in relation to several physiological and pathological mechanisms (Piol et al. 2023; Seo et al. 2022; Cagnetta et al. 2023), no one has so far provided a comprehensive view of the changes that occur at the synaptic level with age. Albeit there is no lack of studies on the modification of the synaptic transcriptome during aging (Chen et al. 2017; Dillman et al. 2017), here we provide the first insight into how transcriptome and proteome change together in the aging synapse. Furthermore, in this work we analyze the effects of aging on differential splicing in the local synaptic proteome. To this end, we analyzed the RNA extracted from synaptosomes obtained from cerebral cortices of C57BL/6J mice of 3 weeks, 5 months, and 18 months of age. These three time points span three pivotal stages of brain development: at 3 weeks corticogenesis is completed, but synaptogenesis is ongoing (Li et al. 2010), and cortical plasticity is likely at its peak (Gordon and Stryker 1996). At 5 months the mouse is considered a mature adult, and this represents an intermediate time point between development and aging. Mice at 18 months of age already suffer from cognitive decay (Fukushima et al. 2008; Peleg et al. 2010), but age-dependent mortality for the BL6 strain is still marginal, with survivorship of around 80% (Flurkey et al. 2007). Synaptosomes are artificial, membranous sacs that contain synaptic components and are generated by subcellular fractionation of homogenized or ground-up nerve tissue because the lipid bilayers naturally reseal together after the axon terminals are torn off by the physical shearing force of homogenization. Synaptosomes contain the complete presynaptic terminal, including mitochondria and synaptic vesicles, along with the postsynaptic membrane and the postsynaptic density (PSD) (Daniel et al. 2012). This preparation has been widely used for biochemical characterization of synapses and to study mechanisms of neurotransmitter release (Trebesova and Grilli 2023; Garcia-Sanz et al. 2001). Here we employ RNA-seq, proteomics, and sequencing of ribosome-associated RNAs to obtain the first multiomics analysis of the aging synapse.

2 | Results and Discussion

2.1 | Synaptosomes Enrichment From Mouse Cortex During Aging

We extracted cortex-derived synaptosome (SYN) samples from young (3 weeks old), adult (5 months old), and old (18 months old) C57BL/6J mice (Table S1). From each sample, both RNA and proteins were purified. The enrichment of synaptic components in SYN samples was verified through Western Blot and quantitative Real-Time PCR (qPCR) (Figure S1A–G).

We then performed depletion of rRNAs and single-end RNA-Seq on SYN and total homogenate (TH) samples, obtaining an average number of reads per sample of 25 ± 1 and 20 ± 3 millions, respectively. The distribution of reads mapping to different genomic features differs between SYN and TH, with higher percentage of reads mapping to intronic sequences in TH samples as compared to SYN samples (Figure S1H), as expected due to the presence of pre-mRNAs in TH. A total of 32,978 (19,097 coding) and 27,905 (17,911 coding) transcripts were detected with at least one read in TH and SYN, respectively. We also measured protein abundances by mass spectrometry-based proteomics and Data Independent Acquisition (DIA). A total of 4083 and 3221 proteins were detected with non-null peptide absolute intensity in TH and SYN, respectively. The percentage of proteins for which also the corresponding transcript was detected is 77% in TH ($N = 3176$) and 98% in SYN ($N = 3168$).

Principal component analysis (PCA) (Figures S1I and S2) visualized three levels of sample separation based on global transcript and protein expression. TH and SYN samples are separated on PC 1 (89% and 52% of variance explained, respectively, for transcripts and proteins), demonstrating that the subcellular origin of samples is the major source of expression variation. The lower separation of TH and SYN at the protein level could represent a biological phenomenon suggesting a more homogeneous protein composition across the ages or could be due to the much lower depth of the data generated by proteomics as opposed to transcriptomics. The respective enrichment in SYN of synaptic proteins and transcripts and depletion of nuclear proteins and transcripts for each of the three age steps was further confirmed by computing the probability distribution functions of the enrichment scores and visualizing them as density plots for these two gene and protein sets (Figure S1J,K). We further assessed the quality of our SYN preparation by comparing our transcriptomic and proteomic data with four public synaptosomal datasets and detected significant positive correlation in all three comparisons (Ouwenga et al. 2017; You et al. 2015; Zappulo et al. 2017; Moczulska et al. 2014) (Table S2 and Figure S3), even when only nonsynaptic proteins were taken into account. As further validation steps, we compared our RNA-seq data with Hafner et al. (2019) paper where synaptosomes were further divided into Vglut+ synaptosomes (excitatory synapses) and Vglut− synaptosomes (inhibitory synapses and glial components), and the analysis showed a clear enrichment of glutamatergic transcripts (Figure S3E). In addition, we compared our proteomics data with Sharma et al. (2015) that identifies cell-type specific proteomes in the brain. The proteins significantly enriched ($FC > 2$) in neurons, oligodendrocytes, astrocytes, and microglia were compared with SYN enriched proteins. Neuronal proteins showed the highest enrichment followed by microglia-specific proteins (Figure S3F).

2.2 | Ribosomal Proteins Are Translationally Repressed in Synaptosomes

We selected genes whose respective transcript and protein levels are differentially expressed in either direction between

SYN and TH in adult animals (adjusted p value > 0.05, Fisher's meta-analysis) (Lury 1972). This selection left 2717 pairs of matched proteins and transcripts. Synaptosomal enrichment/depletion at both protein and transcript levels for these genes is reported as a scatter plot in Figure 1A. The first quadrant of this plot contains genes whose transcript and protein products show synaptic enrichment; notably, this quadrant shows an enrichment of genes coding for synaptic proteins, as shown also in Figure 1D. This quadrant also shows a mild enrichment for endosomal and cytoskeletal genes (Figure S4A–C), which is consistent with the report that they act as scaffolds for local RNA translation (Cioni et al. 2018). The third quadrant contains genes that show synaptic depletion of both the respective transcript and protein; the overrepresented GO categories within this gene set show the expected relation to nuclear proteins (Figure 1D). The second and the fourth quadrants contain genes whose corresponding proteins and transcripts show opposite directions of enrichment. The second quadrant contains synaptically depleted proteins whose transcripts are enriched in the synaptosome. The overrepresented GO categories of this gene set correspond mainly to organelles such as the mitochondrion and the ribosome, in line with previous studies (Figure 1D). These likely correspond to transcripts that are translationally repressed or proteins whose

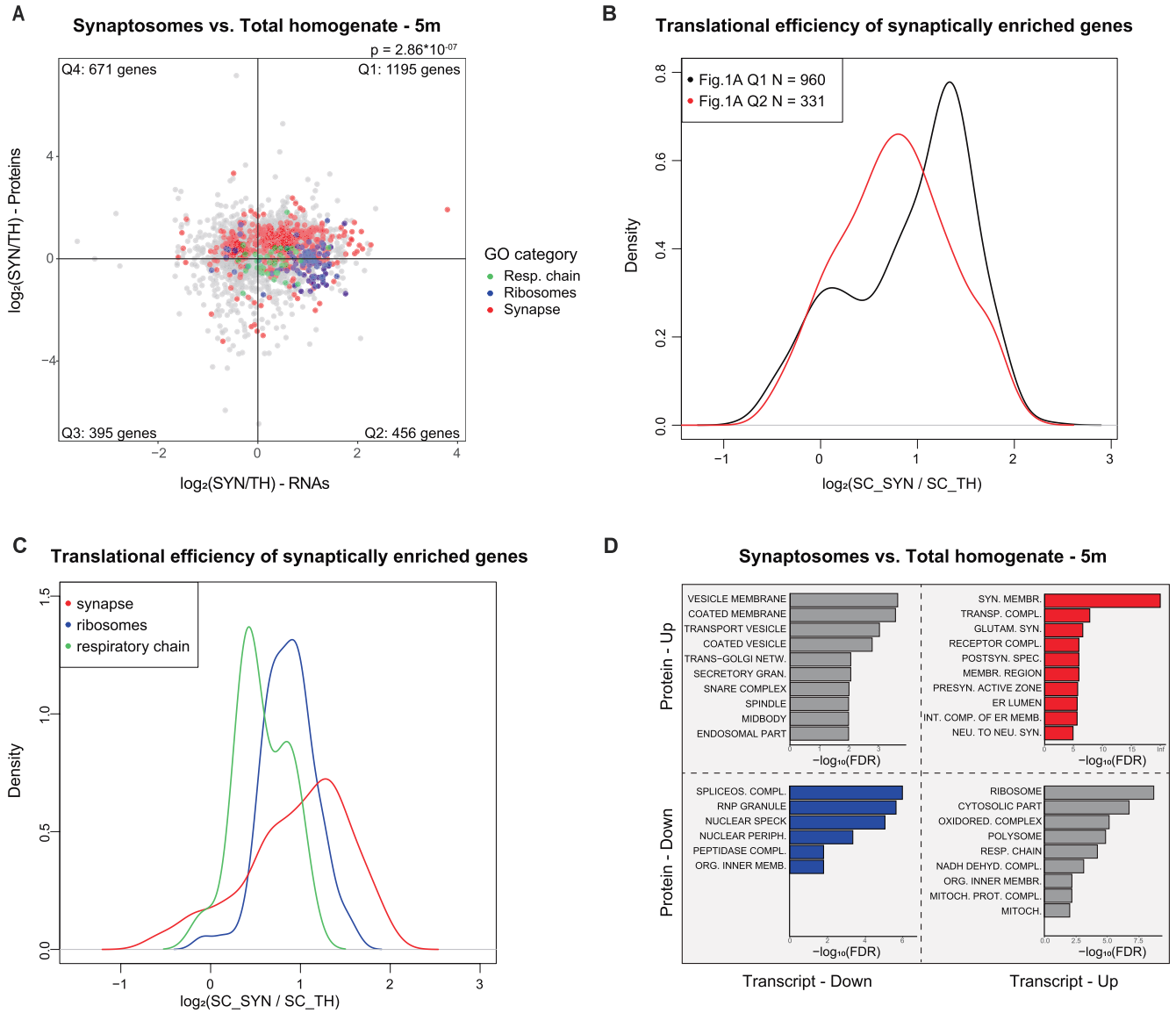

FIGURE 1 | Synaptosomes are enriched in transcripts coding for synaptic proteins. (A) Proteins and RNAs enrichment are plotted as log of the ratio synaptosome vs. total homogenate. Quadrants are named clockwise, starting from the upper right one. The distribution of genes in each quadrant is not uniform according to Fisher's exact test ($p = 2.86 \times 10^{-07}$). Protein and RNA fold changes are correlated using Spearman's correlation ($\rho = 0.141$, $p = 1.342 \times 10^{-13}$). Genes belonging to specific Gene Ontology (GO) terms are highlighted in different colors, red = synapses, blue = ribosome, green = respiratory chain as indicated also in the legend. TH = total homogenate, SYN = synaptosomes. (B) The ratio between ribosome-associated transcripts (translatome) in SYN and TH of genes of Quadrant I and II of Panel A is visualized in form of density plot. The means are significantly different according to Wilcoxon Test (p value = 2.546×10^{-06}). (C) Probability density plot of the translational efficiency of genes in Panel A. Genes belonging to specific Gene Ontology (GO) terms are highlighted in different colors, red = synapses, blue = ribosome, green = respiratory chain as indicated also in the legend. Differences in means are significant according to Kruskal–Wallis Test ($p = 0.0001$). (D) Top10 GO categories significantly enriched in each of the 4 quadrants of Panel (A). Overrepresentation analysis (ORA) was performed with WebGestalt.

half-lives are shorter in the synapses. The fourth quadrant contains proteins enriched in SYN whose transcripts are more abundant in TH. They are enriched for terms related to vesicle components that are involved in soma processes trafficking or in synaptic vesicle trafficking (Figure 1D and Figure S4D). The proteins found in this quadrant are possibly synthesized at the somatic level and transported to the neuronal processes. In fact, it has been extensively reported that synaptic vesicle (SV) proteins are synthesized at the somatic level and transported to the presynaptic terminal along the axon (Hafner et al. 2019; Ahmari et al. 2000; Tao-Cheng 2020; Watson et al. 2023). When projecting the mRNAs identified by Hafner et al. in the Vglut+ synaptosomes on the plot of Figure 1A, it is evident that Q4 contains mRNAs depleted from Vglut+ synaptosomes, but not mRNAs enriched in Vglut+ synaptosomes (Figure S4E). Additionally, to exclude that the higher protein abundance in Q4 might be due to a longer protein half-life, we compared protein half-lives of Q4 and Q1 using data generated from Fornasiero et al. (2018) in mouse cortical synaptosomes. As reported in Figure S4F, we did not detect any difference between the two quadrants. To confirm that transcripts in the second quadrant of Figure 1A (i.e., transcript enriched and protein depleted) are translationally repressed, we performed ribosome pull-down both from SYN and TH, using a Sucrose Cushion (SC). We then isolated ribosome-associated RNA and performed RNA-seq after rRNA depletion, obtaining an average number of reads of 39.6 ± 3.6 million. We then calculated the translational efficiency (TE) by dividing RPKMs of ribosome-associated RNAs in SYN (SC_SYN) by RPKMs of ribosome-associated RNAs in TH (SC_TH). The probability distribution functions of TE of genes belonging to the first and second quadrants of Figure 1A were estimated by Gaussian kernel density and are reported as density plots in Figure 1B. We found that genes of the second quadrant are significantly less associated with ribosomes as compared to genes of the first quadrant (p value $= 2.546 \times 10^{-06}$, estimated by Wilcoxon Test). We also analyzed specifically TE of synaptically enriched genes belonging to the GO categories ribosomes (GO:0005840), respiratory chain (GO:0070469), and synapse (GO:0045202) (Figure 1C). It is apparent that translation is higher for synaptic transcripts, which are all actively translated at the synaptic level as compared to genes belonging to ribosome and respiratory chain categories.

We repeated the comparison between the proteome and transcriptome of SYN and TH using the same procedure used for the other two time points, yielding, respectively, 3142 and 3062 pairs of matched proteins and transcripts in adult and old animals (Figure S5A,E). No substantial change in the genes enriched at the synaptic level was observed during aging (Figure S5D,H). The most relevant changes in GO categories affect genes that are enriched at the transcript but not protein level in synaptosomes (located in the second quadrant). Although these genes appear to have a lower TE compared to those located in Q1, also in young and old animals (Figure S5B,F), GO categories related to ribosomes and the respiratory chain are overrepresented in the second quadrant in young and adult animals, but not in old animals. Notably, the respiratory chain GO category is overrepresented in Q3 (Figure S5D,H) at 18 months, indicating that mitochondrial respiration in old animals is impaired both at the somatic and synaptic level. This observation is in line with the general age-dependent decline in mitochondrial function, characterized by decreased oxidative phosphorylation activity and increased oxidative damage in various organs (Srivastava 2017), and at the synaptic level, where a decline in synaptic mitochondrial function contributes to neuronal and synaptic degeneration (Du et al. 2012).

2.3 | Noncoding RNAs Are Enriched in Synaptosomes

Some noncoding RNAs (ncRNAs) are reported to be particularly enriched in synapses (Rybak-Wolf et al. 2014; Chen et al. 2017). In our dataset, we detected 26,431 genes differentially expressed between SYN and TH, 35% of which are annotated as ncRNAs (9397 genes). In particular, 10,871 transcripts, out of which 827 are annotated as ncRNAs, were significantly enriched in SYN. We compared these genes with synaptically localized ncRNAs extracted from three different datasets (You et al. 2015; Ouwenga et al. 2017; Zappulo et al. 2017) and found 51 ncRNAs significantly enriched in synapses in our data and You et al. data (Figure S6A) and 289 noncoding genes significantly enriched in the synaptic compartment in both our dataset and Zappulo et al. dataset (Figure S6C). As expected, we only found 9 ncRNAs enriched in SYN both in our dataset and Ouwenga et al. TRAP-seq data (Figure S6B), as this dataset is particularly enriched in ribosome-bound transcripts. We confirmed that ncRNAs significantly enriched in SYN ($N = 827$) are translationally repressed by comparing them with Zappulo et al. Ribo-seq data, using as control protein-coding RNAs that are significantly enriched in SYN ($N = 4083$). Probability distribution functions of translation rates were estimated by Gaussian kernel density and are reported as density plots in Figure S6D. Synaptic enrichment of some long ncRNAs was further validated by qPCR (Figure S6E–G).

2.4 | RNA-Protein Decoupling in Aging Synaptosomes

To gain insights on the relationship between transcript and protein abundance, we performed Spearman's correlation between RNA Reads Per Kilobase Million (RPKMs) and the corresponding protein absolute intensities for each time point separately for TH and SYN. We detected a significantly higher correlation in total homogenate as opposed to synaptosomes ($p = 0.0002$ evaluated by two-way ANOVA), likely due to the transport of some proteins from the soma. We also observed a decrease in correlation as a function of age ($p < 0.0001$ evaluated by two-way ANOVA) (Figure 2A), indicating age-dependent decoupling between protein and transcript, as previously observed in total brain homogenates of primates and killifish (Kelmer Sacramento et al. 2020; Wei et al. 2015). To analyze transcript and protein regulation during aging in TH and SYN, we computed Spearman's correlation of RPKMs or protein absolute intensities with age for each gene. Rho coefficients were analyzed using Generally Applicable Gene Enrichment (GAGE) (Luo et al. 2009) to obtain Gene Ontology categories enriched for genes whose expression is positively or

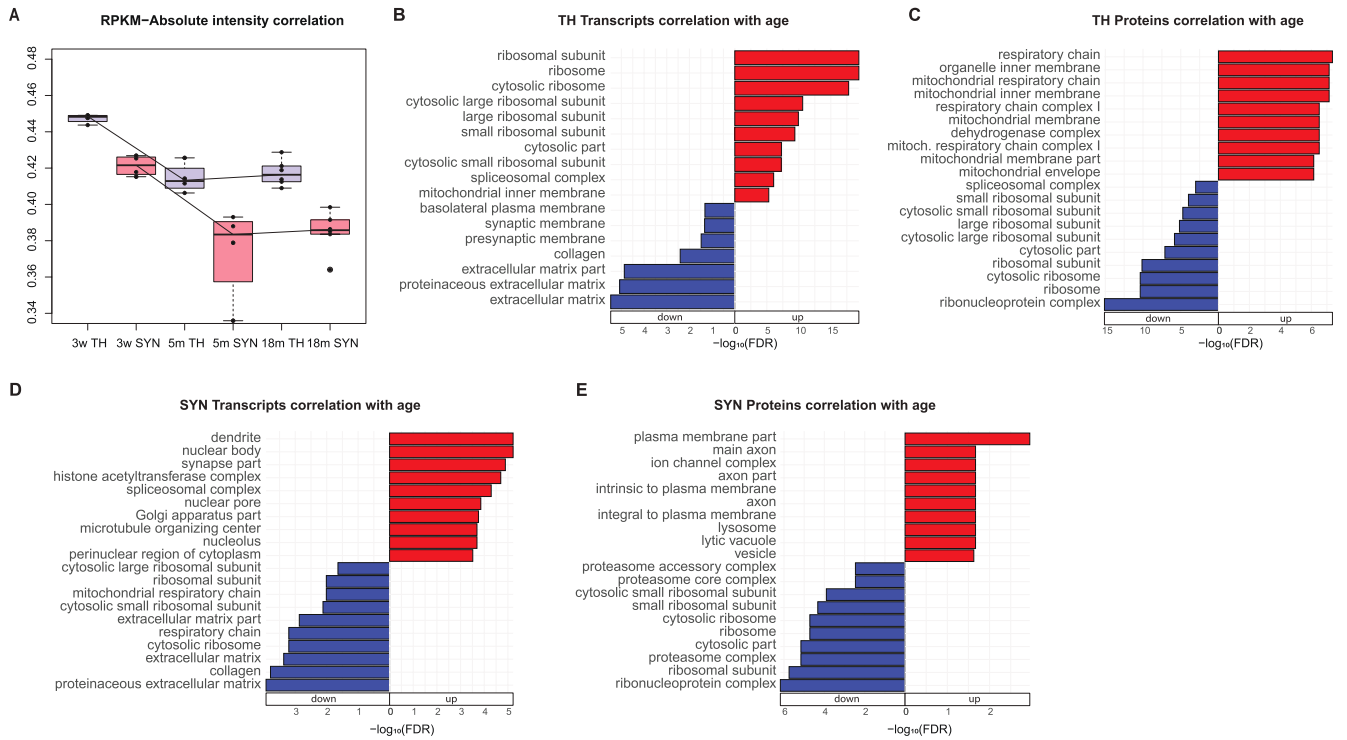

FIGURE 2 | Age-dependent regulation of protein and transcript. (A) Box plot of the proteome-wide correlation between transcript RPKMs and protein absolute intensities in total homogenate (TH) samples, colored in blue and synaptosomal (SYN) samples, colored in red, at 3 weeks, 5 months, and 18 months. Differences between conditions were evaluated by two-way ANOVA. (B) Generally Applicable Gene Enrichment (GAGE) of the correlation of TH transcripts with age. Only the top10 Cellular Component terms are shown. (C) GAGE of the correlation of TH proteins with age. Only the top10 Cellular Component terms are shown. (D) GAGE of the correlation of SYN transcripts with age. Only the top10 Cellular Component terms are shown. (E) GAGE of the correlation of SYN proteins with age. Only the top10 Cellular Component terms are shown.

negatively correlated with age (Figure 2B,C and Figure S7A for TH; Figure 2D,E and Figure S7B for SYN). In TH, transcripts and proteins related to spliceosomal complex and ribosomes display an opposite behavior with aging. At the transcript level, in fact, these genes increase with age, while they decrease with age at the protein level. The same phenomenon of protein-transcript decoupling was observed also in the turquoise killifish *Nothobranchius furzeri* (Sacramento et al. 2019). Some examples are depicted in Figure S7C,D.

We also examined the correlation between age-dependent regulation in SYN and TH during aging, both at the transcriptomic and proteomic levels. The comparison of transcripts regulated between the young and adult stages in SYN and TH yielded 2878 genes significantly regulated in either of the two compartments. The fold change of these genes in total homogenate and synaptosomes is highly correlated ($\rho = 0.811$, p value $< 2.2 \times 10^{-16}$ calculated with Spearman's correlation), suggesting that transcript changes in the synapse are driven by the soma (Figure 3A). The same process was repeated for transcripts regulated during aging, yielding 4364 genes commonly regulated in the two compartments. During aging, the correlation between TH and SYN drastically decreases ($\rho = 0.038$, p value $= 0.011$, calculated with Spearman's correlation), suggesting that the synaptic compartment becomes decoupled from the soma (Figure 3B). We observed the same phenomenon at the proteome level, with a correlation of the two compartments decreasing from 0.615 (p value $< 2.2 \times 10^{-16}$) during adulthood (Figure 3C) to 0.259 (p value $= 4.174 \times 10^{-16}$) during aging (Figure 3D), and at the level of the translatome, with a correlation of the two compartments decreasing from 0.713 (p value $< 2.2 \times 10^{-16}$) during adulthood (Figure 3E) to 0.146 (p value $= 6.024 \times 10^{-09}$) during aging (Figure 3F). While genes coding for synaptic proteins are, as expected, stably expressed and translated during development both in TH and SYN (Figure S8A,C,E), the genes more affected by the decoupling are those coding for ribosomal proteins. More specifically, their transcripts increase, and their proteins decrease in TH while the opposite is observed in SYN (Figure S8B,D, respectively). To further corroborate this finding, we repeated this analysis using the intersection of the adjusted p value, instead of combining them with Fisher's metanalysis. We observed that increasing gene selection stringency does not change the detected decrease in correlation between TH and SYN. In addition, the GO categories overrepresented in the four quadrants are largely consistent (Figure S9).

To explore further the age-dependent transcriptome/proteome decoupling, we analyzed the correlation between RNA and proteins during development and aging, both in TH (Figure 4A,D, Figure S10A,B) and SYN (Figure 4G,J, Figure S10C,D), highlighting in the scatterplots the GO categories that are most affected by aging, namely respiratory chain and ribosome. This correlation decreases from 0.221 (p value $< 2.2 \times 10^{-16}$) to −0.011 (p value $= 0.743$) in TH and from 0.236 (p value $< 2.2 \times 10^{-16}$) to 0.028 (p value $= 0.246$) in SYN. We thus calculated a decoupling score for each gene defined as the ratio between protein and transcript changes:

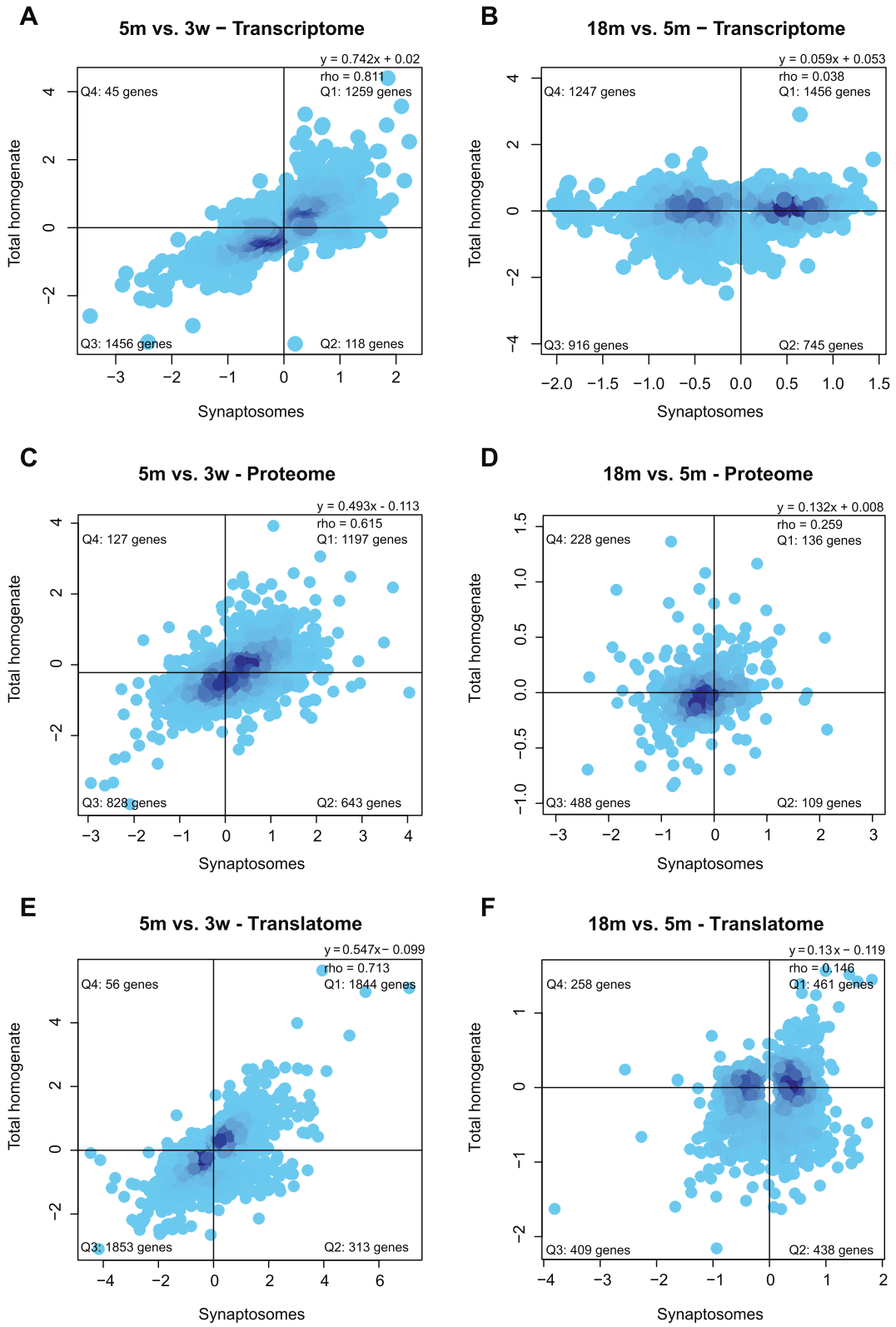

FIGURE 3 | Legend on next page.

positive decoupling indicates that the protein increases more (or is reduced less) than expected from transcript regulation and negative decoupling that the protein increases less (or decreases more) than expected from transcript regulation (Di Fraia et al. 2023) and used decoupling scores of each gene as input for GAGE (Figure 4B,E,H,K). This analysis showed that ribosomal genes have a negative decoupling during development and aging in TH. In SYN, on the other hand, ribosomal genes show a negative decoupling during development and a positive decoupling during aging. Analysis of the correlation of decoupling with changes in translational efficiency (TE) in old SYN confirmed that positive decoupling correlates with

FIGURE 3 | Soma-synapse decoupling during aging. (A) Transcript regulation plotted as log of the ratio 5m vs. 3w in TH and SYN. Quadrants are named clockwise, starting from the upper right one. The distribution of genes in each quadrant is not uniform according to Fisher's exact test ($p < 2.2 \times 10^{-16}$). SYN and TH fold changes are correlated based on Spearman's correlation ($\rho = 0.811$, $p < 2.2 \times 10^{-16}$). (B) Transcript regulation plotted as log of the ratio 18m vs. 5m in TH and SYN. Quadrants are named clockwise, starting from the upper right one. The distribution of genes in each quadrant is not uniform according to Fisher's exact test ($p = 7.856 \times 10^{-09}$). SYN and TH fold changes are weakly correlated using Spearman's correlation ($\rho = 0.038$, $p = 0.011$). (C) Protein regulation plotted as log of the ratio 5m vs. 3w in TH and SYN. Quadrants are named clockwise, starting from the upper right one. The distribution of genes in each quadrant is not uniform according to Fisher's exact test ($p < 2.2 \times 10^{-16}$). SYN and TH fold changes are correlated using Spearman's correlation ($\rho = 0.615$, $p < 2.2 \times 10^{-16}$). (D) Protein regulation plotted as log of the ratio 18m vs. 5m in TH and SYN. Quadrants are named clockwise, starting from the upper right one. The distribution of genes in each quadrant is not uniform according to Fisher's exact test ($p = 9.909 \times 10^{-11}$). SYN and TH fold changes are correlated using Spearman's correlation ($\rho = 0.259$, $p = 4.174 \times 10^{-16}$). (E) Ribosome-associated transcript regulation plotted as log of the ratio 5m vs. 3w in TH and SYN. Quadrants are named clockwise, starting from the upper right one. The distribution of genes in each quadrant is not uniform according to Fisher's exact test ($p < 2.2 \times 10^{-16}$). SYN and TH fold changes are correlated using Spearman's correlation ($\rho = 0.713$, $p < 2.2 \times 10^{-16}$). (F) Ribosome-associated RNAs transcript regulation plotted as log of the ratio 18m vs. 5m in TH and SYN. Quadrants are named clockwise, starting from the upper right one. The distribution of genes in each quadrant is not uniform according to Fisher's exact test ($p = 8.305 \times 10^{-07}$). SYN and TH fold changes are correlated using Spearman's correlation ($\rho = 0.146$, $p = 6.24 \times 10^{-09}$).

an increase in TE and that higher protein concentration is the result of higher rates of protein synthesis (Figure 4L).

We confirmed that ribosomal proteins decrease in TH and increase in SYN during aging by a Western blot in an independent group of samples (Figure 5A,B and Figure S11, $p = 0.243$ for SYN and $p = 1.6 \times 10^{-11}$ for TH evaluated by two-way ANOVA). Similarly, the decrease of transcripts coding for ribosomal proteins in SYN was confirmed by means of qPCR while regulation of transcripts in TH was not consistent (Figure 5C, $p = 8.97 \times 10^{-11}$ for SYN and 0.0273 for TH evaluated by two-way ANOVA). Moreover, we evaluated the amount of ribosomal RNA (rRNA) with a bioanalyzer (Figure 5D). This datum indicates that higher ribosomal proteins correlate with an increase in fully assembled ribosome at the synaptic level. We also performed targeted proteomics via Parallel Reaction Monitoring (PRM) of ribosomal proteins in our SYN samples (Table S3). We observed a significant increase (evaluated by one-way ANOVA) of two of the four analyzed proteins in adult and aged SYN (Figure 5E). Finally, a staining of a ribosomal protein and RNA on isolated synaptosomes (Richter et al. 2018) further corroborated our data (Figure 5F, $p < 0.0001$ evaluated by Kruskal–Wallis test).

To analyze which changes occur in posttranslational modifications at the synaptic level, we compared the Differentially Expressed Proteins (DEPs) with a recently published work on posttranslational modifications in the brain (Marino et al. 2025). This comparison revealed that phosphorylation is generally reduced among downregulated synaptic (SYN) DEPs. In addition, we observed a global downregulation of acetylation and an upregulation of ubiquitination across synaptic DEPs, independent of whether the proteins themselves were up- or downregulated (Figure S12).

2.5 | Differential Expression of Transcript Isoforms in Aging Synaptosomes

In order to identify transcript isoforms that are differentially expressed in SYN with aging, we performed paired-end long read sequencing on TH and SYN from young, adult, and old mice of ages corresponding to the previous experiments. We applied both DIEGO (Doose et al. 2018) and LeafCutter (Li et al. 2018). In both cases, Differentially Expressed Junctions (DEJs) were identified for each of the age comparisons SYN 3w/5m, SYN 3w/18m, and SYN 5m/18m. Both software identify transcript isoforms by determining differentially expressed junctions based exclusively on split-read information and do not make use of a priori gene models, like DEXSeq (Anders et al. 2012). The two software, however, use different methods for the detection of statistically significant DEJs. DIEGO analyzes each splice junction separately and assigns a q-value to its differential usage. LeafCutter analyzes clusters, that is, a set of junctions connected to each other through common acceptor or donor splice sites, and assigns an adjusted p value to each cluster based on differential connectivity within the cluster. In the three age comparisons, 3099, 1496, and 2192 DEJs (DIEGO) and 4249, 4175, and 4036 clusters (LeafCutter) were identified, respectively. Both software identified only a negligible number of DEJs that could not be mapped to an annotated gene or that spanned an unrealistically large range (> 106 bp). For each age comparison, we evaluated the percentage of DEJs with either: (i) both donor and acceptor splice sites annotated, (ii) only one of the two splice sites annotated, and (iii) both splice sites unannotated (Figure S13A,B). LeafCutter-identified more junctions with at least one unannotated splice site compared to DIEGO (18.74% in LeafCutter and 8.95% in DIEGO, on average). Next, we evaluated the percentage of DIEGO-derived DEJs (Figure S13C) and LeafCutter-derived clusters (Figure S13D) mapping on the 5′UTR, on the coding sequence (CDS), on the 3′UTR, and on the introns. Most splice sites map to the UTRs and the CDS; however, we detected a higher percentage of LeafCutter-identified splice sites mapping on the 5′UTR and on introns, suggesting either that LeafCutter identifies more unannotated exons and 5′UTR isoforms or that it has a higher rate of false-positive calls, as compared to DIEGO. We performed GO terms overrepresentation analysis on the top 1000 q-value ranked DIEGO-derived DEJs (Figure S12E–G) and on the top 1000 adjusted p value ranked LeafCutter-derived clusters (Figure 6A–C) to gain insights into the function of age-dependent differentially spliced synaptic transcripts. The GO category GTPase binding (GO:0051020) resulted preeminent in all three comparisons. GTPase activity is involved in a multitude of processes that are important in synaptic function, like signal transduction at the level of G protein-coupled receptors,

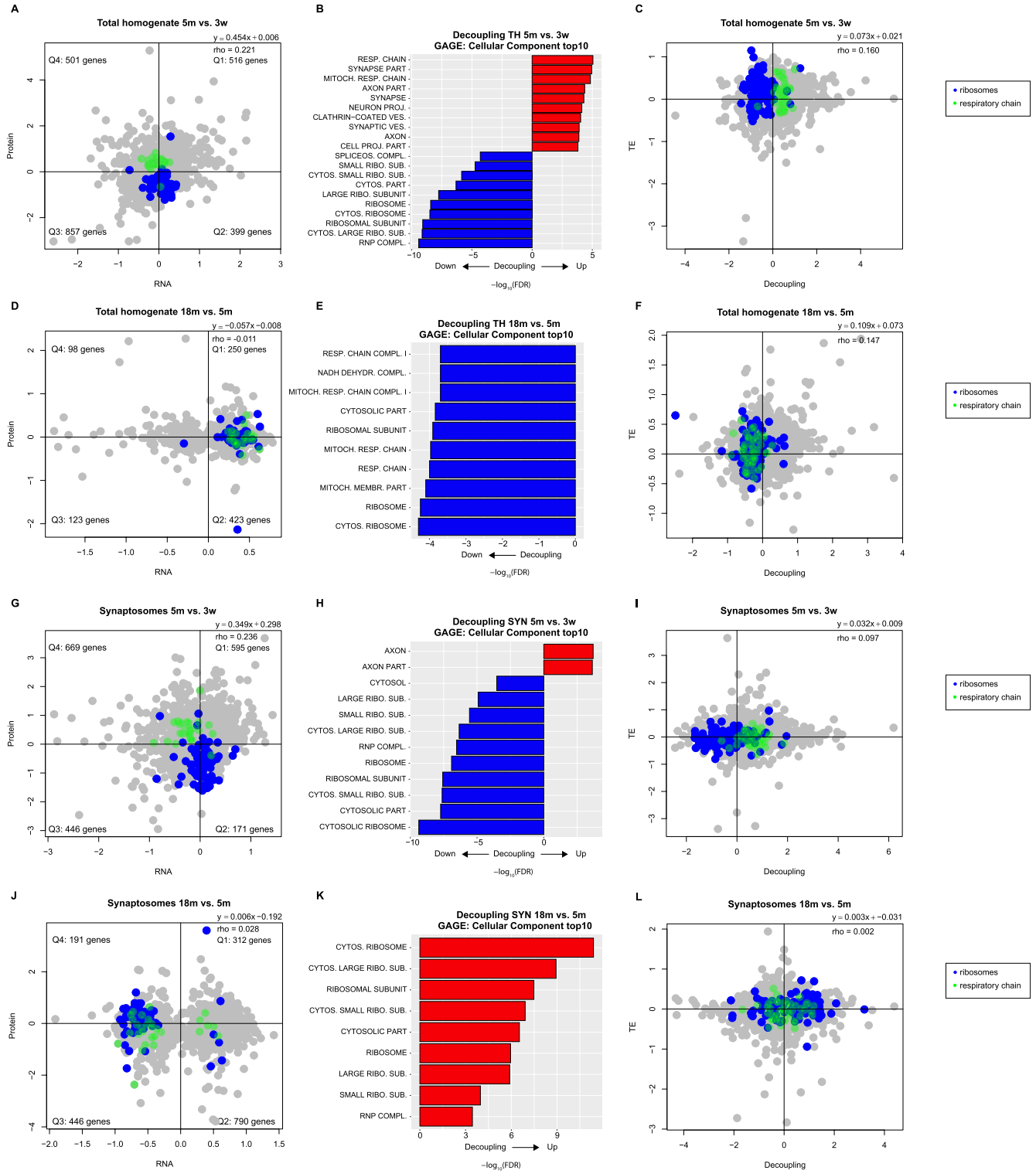

FIGURE 4 | Legend on next page.

neurotransmitter release, protein synthesis, and synaptic plasticity. This enzymatic activity is regulated by various GTPase binding proteins, like guanine nucleotide exchange factors (GEFs), which catalyze the exchange of GDP with GTP and the reactivation of the GTPase; GTPase activating proteins (GAPs), which increase the GTPase activity; and guanosine nucleotide dissociation inhibitors (GDIs) that inhibit the exchange of GDP with GTP and therefore maintain the GTPase in its inactive state.

Furthermore, we compared the overlap between the GO categories enriched in the DEGs (adjusted p value <0.01) and in the genes that contain DEJs identified both with DIEGO (top 1000 q value ranked DEJs) and LeafCutter (top 1000 adjusted p value ranked clusters) (Figure S13H–J and Figure 6D–F). We observed a larger overlap between DEGs and DEJs in the contrast SYN 3w versus 5m as compared to the contrast SYN 5m versus 18m, with only 10.7% (60/558) DEJs not DEG (Figure 6D) as opposed

FIGURE 4 | Transcriptome/proteome decoupling with aging in TH and SYN. (A) Proteins and RNAs enrichment in TH are plotted as log of the ratio 5m vs. 3w. Quadrants are named clockwise, starting from the upper right one. The distribution of genes in each quadrant is not uniform according to Fisher's exact test ($p < 2.2 \times 10^{-16}$). Protein and RNA fold changes were correlated using Spearman's correlation ($\rho = 0.221$, $p < 2.2 \times 10^{-16}$). Genes belonging to specific Gene Ontology (GO) terms are highlighted in different colors, blue = ribosome, green = respiratory chain as indicated also in the legend. (B) Generally applicable gene enrichment (GAGE) of the decoupling of transcripts and proteins in TH during development. Positive decoupling indicates higher protein level than expected from transcript regulation and negative decoupling less protein level than expected from transcript regulation. Only the top10 categories ranked on $\log_2$ of the p value are shown. (C) Decoupling and Translational Efficiency (TE) in TH are plotted as log of the ratio 5m vs. 3w. Decoupling and TE fold changes were correlated using Spearman's correlation ($\rho = 0.160$, $p < 2.2 \times 10^{-16}$). Genes belonging to specific Gene Ontology (GO) terms are highlighted in different colors, blue = ribosome, green = respiratory chain as indicated also in the legend. (D) Proteins and RNAs enrichment in TH are plotted as log of the ratio 18m vs. 5m. Quadrants are named clockwise, starting from the upper right one. The distribution of genes in each quadrant is uniform according to Fisher's exact test ($p = 0.0673$). Protein and RNA fold changes were not significantly correlated according to Spearman's correlation ($\rho = -0.011$, $p = 0.743$). Genes belonging to specific Gene Ontology (GO) terms are highlighted in different colors, blue = ribosome, green = respiratory chain as indicated also in the legend. (E) GAGE of the decoupling of transcripts and proteins in TH during aging. Only the top10 categories are shown. (F) Decoupling and TE in TH are plotted as log of the ratio 18m vs. 5m. Decoupling and TE fold changes were correlated using Spearman's correlation ($\rho = 0.147$, $p < 2.2 \times 10^{-16}$). Genes belonging to specific Gene Ontology (GO) terms are highlighted in different colors, blue = ribosome, green = respiratory chain as indicated also in the legend. (G) Proteins and RNAs enrichment in SYN are plotted as log of the ratio 5m vs. 3w. Quadrants are named clockwise, starting from the upper right one. The distribution of genes in each quadrant is not uniform according to Fisher's exact test ($p = 6.165 \times 10^{-16}$). Protein and RNA fold changes were correlated using Spearman's correlation ($\rho = 0.236$, $p < 2.2 \times 10^{-16}$). Genes belonging to specific Gene Ontology (GO) terms are highlighted in different colors, blue = ribosome, green = respiratory chain as indicated also in the legend. (H) GAGE of the decoupling of transcripts and proteins in SYN during development. Only the top10 categories are shown. (I) Decoupling and TE in SYN are plotted as log of the ratio 5m vs. 3w. Decoupling and TE fold changes were correlated using Spearman's correlation ($\rho = 0.097$, $p = 2.515 \times 10^{-09}$). Genes belonging to specific Gene Ontology (GO) terms are highlighted in different colors, blue = ribosome, green = respiratory chain as indicated also in the legend. (J) Proteins and RNAs enrichment in SYN are plotted as log of the ratio 18m vs. 5m. Quadrants are named clockwise, starting from the upper right one. The distribution of genes in each quadrant is uniform according to Fisher's exact test ($p = 0.475$). Protein and RNA fold changes were correlated using Spearman's correlation ($\rho = 0.028$, $p = 0.247$). Genes belonging to specific Gene Ontology (GO) terms are highlighted in different colors, blue = ribosome, green = respiratory chain as indicated also in the legend. (K) GAGE of the decoupling of transcripts and proteins in SYN during aging. Only the top10 categories are shown. (L) Decoupling and TE in SYN are plotted as log of the ratio 18m vs. 5m. Decoupling and TE fold changes were correlated using Spearman's correlation ($\rho = 0.002$, $p = 0.875$). Genes belonging to specific Gene Ontology (GO) terms are highlighted in different colors, blue = ribosome, green = respiratory chain as indicated also in the legend.

to the contrast SYN 5m versus 18m with 43% (261/605) DEJs not DEG (Figure 6F, $p < 10^{-6}$, Fisher's exact test), suggesting that during aging, regulation of transcript abundance, and alternative splicing become more decoupled. Generally, changes in synaptic transcriptome during aging might be imputable either to changes in the relative expression of certain transcripts (DEGs) or to a transcript isoform switch (DEJs), where the two processes can occur independently. We observed a significant overlap in GO categories enriched in DEGs and genes containing DEJs when comparing SYN of young animals with those of adult and old animals, suggesting that, during development, the same biological processes are modulated via changes in both transcript abundance and transcript isoform. On the other hand, during aging, the two phenomena diverge, indicating that synaptic gene expression might be regulated independently by changes in transcript abundance and changes in transcript isoform.

We selected a subset of DEJs that were preeminent in at least one of the three age comparisons, according to either DIEGO or LeafCutter (Table 1 and Figure S13K–M), and examined the variation in transcript abundance in the three age comparisons (Table 2). Bcas1 and Nfasc showed a marked decrease upon aging, while the other genes were not differentially expressed in the analyzed time points. A summary of the age-dependent protein and transcript isoform changes is shown in Figure 6G–J. The change in the usage of the selected junctions was validated through RT-qPCR (Figure 6K–O') and RT-PCR (Figure S14A–C) using an independent set of samples. In all the considered genes, the junction is differentially used due to differential expression of adjacent exons or of exons spanning that junction; we therefore designed three primer pairs: one amplifying a "normalizer exon," immediately adjacent to the selected junction, one amplifying the junction between the differentially expressed exon and the normalizer exon, and the last one amplifying the entire region in which alternative splicing was detected. For the validation through RT-qPCR, we used the gene *Ldhb* as a normalizer, due to its stable expression, between both TH and SYN at the considered time points.

2.6 | Birc2

BIRC2 is an Inhibitor of Apoptosis Protein (IAP) and inhibits apoptosis by binding Caspases (through BIR domains) and ubiquitinating them (Silke and Meier 2013). By inspecting the read coverage of Birc2, we identified an unannotated exon (to which we will refer to as "Exon 4b") in 3-week SYN. As shown in Table S4 and Figure S14D, split reads span the junction between Exon 4 and Exon 5 and the junction between Exon 4b and Exon 5, but no split read is detectable between Exon 4 and 4b; furthermore, the putative unannotated donor splice site at the 3′ end of exon 4b (GTAAGC) is consistent with the consensus sequence "GTAAGT," thus we hypothesized that an unannotated Transcription Start Site (TSS) might be present at the 5′ end of Exon 4b, generating a transcript isoform that does not include Exons 1–4 and, consequently, a protein with a shorter

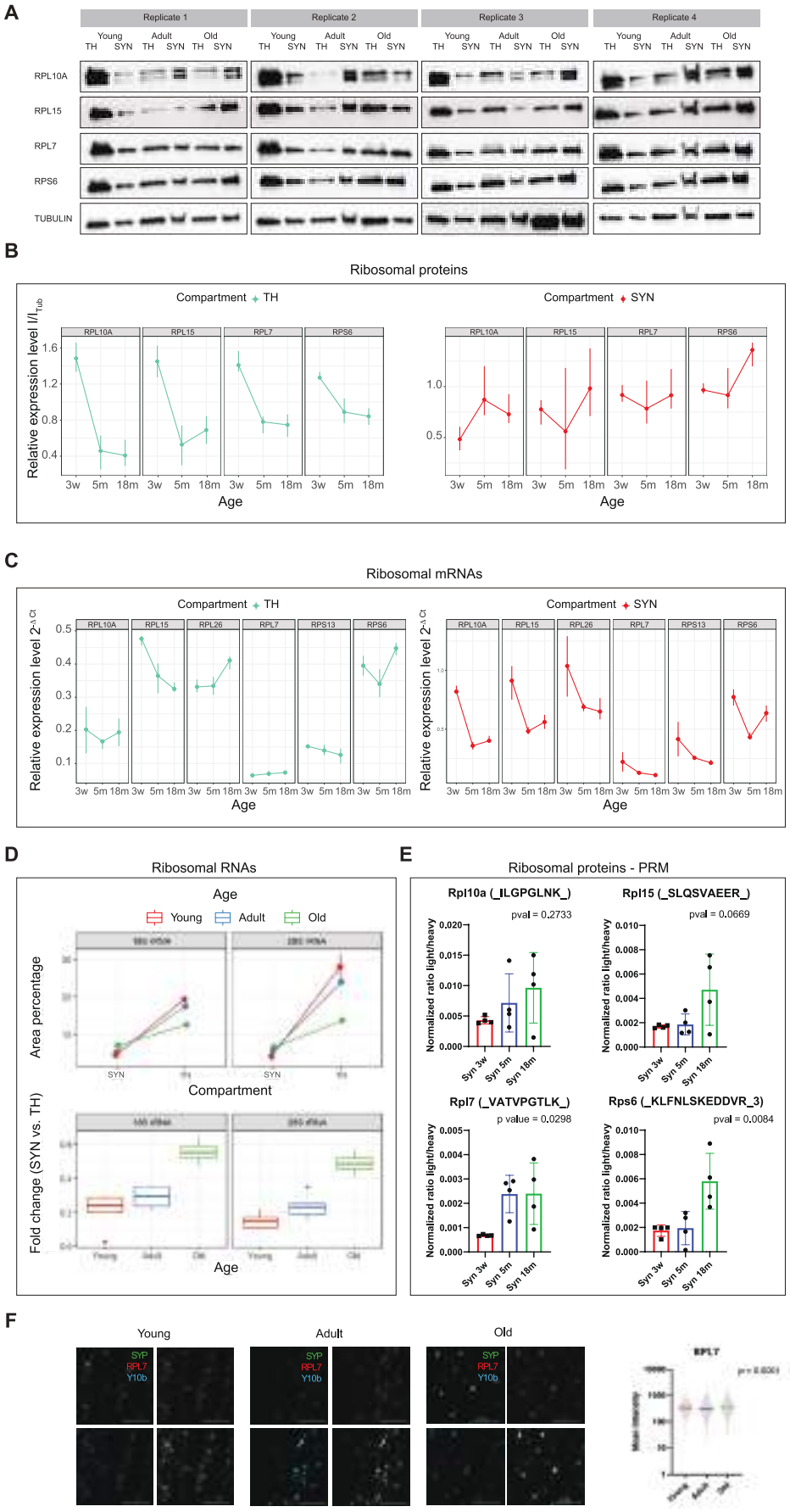

FIGURE 5 | Legend on next page.

FIGURE 5 | Validation of ribosomal transcripts and proteins regulation in synaptosomes during aging. (A) Western blot of ribosomal proteins using total cortical homogenate and synaptosomes of young, adult and old animals. Tubulin was used as loading control in all the experiments. (B) Left panel: Mean of protein intensity quantification in Total Homogenate (TH) relative to tubulin for each time point of panel (A). Right panel: Mean of protein intensity quantification in synaptosomes (SYN) relative to tubulin for each time point of panel (A). (C) Left panel: Mean of ribosomal transcripts expression in total homogenate (TH) relative to Ldhb for each time point using independent samples. Right panel: Mean of ribosomal transcripts expression in synaptosomes (SYN) relative to Ldhb for each time point using independent samples. Each time point $N=4$. (D) Ribosomal RNA (rRNA) in total homogenate (TH) and synaptosomes (SYN). Box plot of the fold change of 18S and 28S between SYN and TH across the ages. Red indicates young animals ($N=4$), blue adult animals ($N=4$) and green old animals ($N=4$). (E) Targeted proteomics of ribosomal proteins in SYN. Normalized ratios of light to heavy peptides displayed. *p* values estimated by one-way ANOVA. (F) Immunofluorescence of SYN isolated from young, adult and old animals ($N=4$ for each time point). Synaptic protein synaptophysin (SYP) stained in green, in red Ribosomal protein RPL7 and in blue Ribosomal RNA. Bar 5 μm. Right panel: Quantification of mean fluorescence intensity of RPL7 using SYP as reference. Each dot represents a single synaptosome, bars indicate the mean with 95% Confidence Interval (CI). (F) Isolated synaptosomes staining. Synaptosomes were immunostained with synaptophysin (SYP) (green), RPL7 (red), and Y10b (blue). On the right the mean intensity of RPL7 channel compared to SYP channel in the three time points is reported ($p<0.0001$ evaluated by Kruskal–Wallis test).

N-terminal. In fact, we were able to identify in Exon 5 a start codon contained in a Kozak sequence and in frame with the open reading frame (ORF) using ATGpr tool (Salamov et al. 1998). In agreement with these results, the amplicon spanning the junction 4b-5 is more expressed in SYN 3w as compared to SYN 5m and SYN 19m, indicating that the unannotated isoform is only present in young synapses (Figure 6K′ and Figure S14A). In the truncated protein isoform, the first 395aa are missing. That means that the three BIR domains are not present in this protein and that only the RING domain (amino acids 565–600) and the CARD domain (amino acids 447–537) remain (Figure 6G), where the latter can inhibit the E3 ubiquitin-protein ligase activity by preventing RING domain dimerization (Lopez et al. 2011). We hypothesize that the loss of function of BIRC2 that results from the loss of its BIR domains facilitates the successful activation of apoptotic signaling in neurons of young animals, which could be important for synaptic pruning and neuronal circuit formation. Alternatively, this truncated protein may act noncanonically and control biological processes other than apoptosis.

2.7 | Bcas1

BCAS1 (Breast Carcinoma Amplified Sequence 1) is a basic protein highly expressed in the brain; its knockout is associated with schizophrenia-like behavioral abnormalities in mice (Fard et al. 2017; Ishimoto et al. 2017). The inspection of the coverage of its transcript (Figure S14E) suggests that Exons 9–11 are more expressed in SYN 3w as compared to SYN 5m and SYN 18m. In agreement with this result, the amplicon spanning the junction 8–9 is higher expressed in young SYN and progressively decreases its expression with aging (Figure 6L′ and Figure S14B). Interestingly, the amplification of the junction 8–12 generates four amplicons, of which only two correspond to the isoforms containing or excluding the Exons 9–11, while the other two might be further variants containing only some of the three exons (Figure S14B). The Exons 9–11 have all lengths multiple of 3 (respectively 42, 165, and 66 nt), and all the possible transcript isoforms are therefore in frame for translation. Therefore, in adult and old synapses, the short-length and the mid-length isoforms are more frequent, while in young synapses, the long-length isoform is the dominant isoform (Figure 6H). Little is known about the structure of the protein and its possible role in synapse physiology. However, various phosphorylation sites are annotated (Huttlin et al. 2010), and some of them are located in the N-terminal region that is coded in isoform 201, but not in isoform 208 transcripts, and in the Exons 9–11. The age-dependent translation of the abovementioned transcript isoforms would therefore lead to peptides with different phosphorylation sites, and that, on the other hand, could have an impact on the protein function.

2.8 | Nfasc

Neurofascin is a cell adhesion molecule of the L1 subgroup of the immunoglobulin superfamily that mediates homophilic adhesions through its Ig-like domains. It mediates axon targeting and synapse formation during neural development, and both glial and neuronal isoforms are known. This transmembrane protein is organized in an N-terminal extracellular region, a transmembrane domain, and a C-terminal cytoplasmic domain. The first 24aa of the N-terminal represent the signal peptide and are therefore absent in the mature protein. The extracellular domain is composed of six Ig-like domains, five Fibronectin type-III (FN III) domains, and one PAT domain, and the various isoforms have different FN III domains and can have or not have the PAT domain (Kriebel et al. 2012; Suzuki et al. 2017). Exon pairs 18–19, 20–21, 22–23, 24–25, and 28–29 (isoform 207) code, respectively, for the FN III Domains 1–5, while the exon pair 26–27 codes for the PAT domain.

This transcript is subject to extensive differential splicing. We identified 18 and 20 DEJs with DIEGO and LeafCutter, respectively, in the three age comparisons, which, if merged by interval overlapping, are organized in six regions along the transcript, of which all but Regions 3 and 5 showed any detectable age-dependent change in coverage. Those regions correspond, respectively, to Exons 26–29 (Region 1), Exons 22–23 (Region 2), Exon 8b (Region 4), and Exon 1 (Region 6). The inspection of the coverage suggests that Exons 26–29 (Region 1) are less expressed in SYN 3w, as compared to SYN 5m and SYN 18m. Furthermore, the inspection of the coverage of exons 22–23 (Region 2) suggests that they are more expressed in SYN 3w, as compared to SYN 5m and SYN 18m. In line with this result, we confirmed that the amplicon spanning the junction 21–22 is expressed the most in SYN 3w (Figure 6M′). The amplification of the region spanning

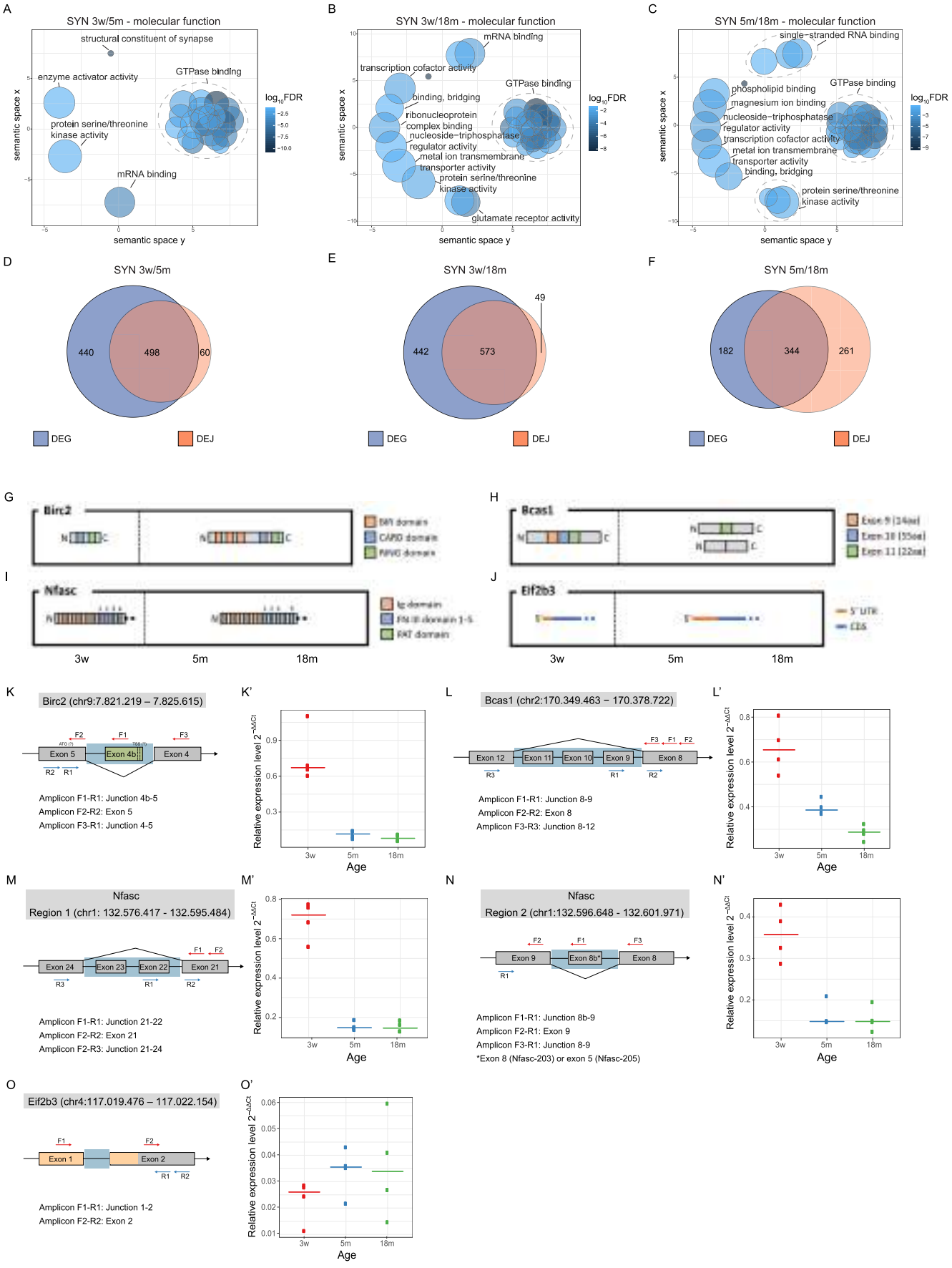

FIGURE 6 | Legend on next page.

FIGURE 6 | Differentially spliced genes (LeafCutter) show overrepresentation of GTPase binding activity and significantly overlap with differentially expressed genes (DEGs) in the same age comparison. (A–C) Gene Ontology (GO) categories (Molecular Function) that are overrepresented in the list of genes to which the 1000 most significant clusters (ranked on adjusted *p* value) map in the three age comparisons SYN 3m vs. 5m (A), SYN 3w vs. 18m (B) and SYN 5m vs. 18m (C) are represented by REVIGO through multidimensional scaling using a measure of semantic dissimilarity (the distances between dots, that represent single GO categories, are inversely related to the similarity of the categories). Ellipses delimit manually identified clusters of highly similar GO categories, and a representative term of each cluster is indicated. (D–F) Overlap of the list of GO categories that are overrepresented in the list of genes to which the 1000 most significant clusters (lowest adjusted *p* value) map (orange) and the list of genes that are differentially expressed (adjusted *p* value < 0.01) (blue) in the three age comparisons SYN 3m vs. 5m (D), SYN 3w vs. 18m (E) and SYN 5m vs. 18m (F). The overlap is highly significant at all three age comparisons but smaller for the SYN 5m vs. 18m comparison, given that both the comparisons 60/498 vs. 261/344 and 49/573 vs. 261/344 are significantly different (Fisher's exact test, *p* value < 0.0001). (G–J) Schematic representation of the predominant protein and transcript isoforms of the three genes *Birc2* (G), *Bcas1* (H), *Nfasc* (I) and *Eif2b3* (J) in young, adult and old synapses. The sizes and distances of the different domains are not to scale. (K–O′) Experimental validation of candidate junction. (K) Schematic representation of the primer pairs used for RT-qPCR and RT-PCR validations for *Birc2*. Please note that the coding sequence of *Birc2* is annotated on the—strand. Exons are represented as gray boxes and introns as black lines (not to scale). The green box represents the unannotated Exon 4b. A light blue background represents the region spanned by the identified DEJ. Putative TSSs and ATG sites are shown, respectively, on Exon 4b and 5. The dotted lines at the 3′ end of Exon 4b indicate that this is not clearly defined. (K′) Validation by RT-qPCR. The relative expression of the Junction 4b-5 is reported as normalized by expression of the Exon 5. (L) Schematic representation of the primer pairs used for RT-qPCR and RT-PCR based validation for *Bcas1*. Please note that the coding sequence of *Bcas1* is annotated on the—strand. Exons are represented as gray boxes and introns as black lines (not to scale). A light blue background represents the region spanned by the identified DEJ. (L′) Validation by RT-qPCR. The relative expression of the Junction 8–9 is reported as normalized by expression of the Exon 8. (M, N) Schematic representation of the primer pairs used for RT-qPCR and RT-PCR based validation of Region 1 and Region 2 of *Nfasc*. Please note that the coding sequence of *Nfasc* is annotated on the—strand. Exons are represented as gray boxes and introns as black lines (not to scale). Light blue backgrounds represent the two regions. (M′, N′) Validation by RT-qPCR. The relative expression of the Junctions 21–22 (M′) and 8b-9 (N′) are reported as normalized by expression of Exons 21 (M′) and 9 (N′). (O) Schematic representation of the primer pairs used for RT-qPCR based validation for *Eif2b3*. Exons are represented as gray boxes and introns as black lines (not to scale). Exons or parts of exons that are part of the 5′UTR are represented in orange. A light blue background represents the region spanned by the identified DEJ. (O′) Validation by RT-qPCR. The relative expression of the Junction 1–2 is reported as normalized by expression of the Exon 2.

TABLE 1 | List of candidate junctions chosen for validation.

Gene name (coordinates)	Comparison	DIEGO	LeafCutter
Birc2 (chr9:7.821.219–7.825.615)	SYN (3w) vs. SYN (5m)	—	$\Delta\Psi = 0.33$ (**)
	SYN (3w) vs. SYN (18m)	—	$\Delta\Psi = 0.33$ (**)
Bcas1 (chr2:170.349.463–170.378.722)	SYN (3w) vs. SYN (5m)	AC = −1.1 (*)	$\Delta\Psi = 0.25$ (***)
	SYN (3w) vs. SYN (18m)	—	$\Delta\Psi = 0.17$ (***)
	SYN (5 m) vs. SYN (18m)	—	$\Delta\Psi = -0.06$ (ns)
Eif2b3 (chr4:117.019.476–117.022.154)	SYN (3w) vs. SYN (5m)	AC = −1.0 (ns)	—

Note: Significance values of *q* value (DIEGO) and adjusted *p* value (LeafCutter) are indicated in the following way: ^{ns}> 0.05, *< 0.05, **< 0.01, ***< 0.001. AC values are rounded to the nearest tenth, *q* value and adjusted *p* value to the nearest thousandth and Psi to the nearest hundredth.
Abbreviation: AC, abundance change.

junctions 21–24 provided a clear result, since we were able to observe two bands, corresponding to the isoforms with and without Exons 22–23, of which only the first one is amplified in SYN 3w (Figure S14C). Those results suggest that the predominant transcript isoform in young synapses does not code for the 5th FN III domain and the PAT domain (Exons 26–29 less expressed), while the predominant transcript isoform in adult and old synapses does not code for the 3rd FN III domain (Exons 22–23 less expressed). This suggests that in young synapses the predominant transcript isoform codes for NF155, while in adult and old synapses the predominant transcript isoform codes for NF186 (Figure 6I). In fact, it is known that the isoform NF155 is the glial isoform, which is expressed with the onset of myelination, while the isoform NF186 is predominantly expressed in the adult brain, where it stabilizes axo-axonic synapses and mediates the clustering of Na_v channels (Kriebel et al. 2012).

Furthermore, when we inspected the coverage of Region 4, we hypothesized that Exon 8b (51 nt) could be more expressed in SYN 3w, compared to SYN 5m and SYN 19m. In agreement with this result, the amplicon spanning the junction 8b-9 resulted to be more expressed in SYN 3w, both in RT-qPCR and RT-PCR (Figure 6N and Figure S14C). The amplification of the region spanning the junction 8–9 generates three different amplicons, of which two correspond to the isoforms with and without Exon 8b. The first one is slightly more expressed in SYN 3w, while the second one is clearly expressed the most in SYN 3w. The third amplicon (slightly longer than 200 bp) might represent an unspecific amplification, given that no

TABLE 2 | Log_2 fold change (log_2FC) and the corresponding adjusted *p* values of the candidate genes in the three age comparisons SYN 3m vs. 5m, SYN 3w vs. 18m and SYN 5m vs. 18m.

	SYN (3w) vs. SYN (5m)	SYN (3w) vs. SYN (18m)	SYN (5m) vs. SYN (18m)
Birc2	$log_2FC = 0.17$ (ns)	$log_2FC = 0.31$ (ns)	$log_2FC = 0.13$ (ns)
Bcas1	$log_2FC = 0.87$ (***)	$log_2FC = 1.11$ (***)	$log_2FC = 0.24$ (ns)
Nfasc	$log_2FC = 1.31$ (***)	$log_2FC = 1.20$ (***)	$log_2FC = -0.12$ (ns)
Eif2b3	$log_2FC = -0.38$ (ns)	$log_2FC = -0.08$ (ns)	$log_2FC = 0.29$ (ns)

Note: Adjusted *p* values are indicated in the following way: $^{ns} > 0.05$, $* < 0.05$, $** < 0.01$, $*** < 0.001$. Log_2FC values are rounded to the nearest hundredth.

third splicing isoform can be observed from the coverage data. Given that this region codes for a part of the portion between the 2nd Ig-like domain (Exons 7–8) and the 3rd Ig-like domain (Exons 9–10), it seems that the predominant transcript isoform in young synapses codes for a 17 aa longer variant of this protein segment.

Finally, we evaluated Region 6, noticing that two 5′UTR isoforms could be observed: an Nfasc-202/-203 isoform (286/292 nt), that can be observed at all three ages, and an Nfasc-201 isoform (427 nt), that can be observed only in young synapses (Figure S14F). The biological function of these two different 5′UTRs, and the underlying alternative TSSs, has not been inquired yet.

2.9 | Eif2b3

EIF2B is the GEF that catalyzes the reactivation of eIF2alfa, and EIF2B3 is its third (gamma) subunit. The inspection of the coverage of its transcript suggests that Exon 1, which is part of the 5′UTR, is less expressed in SYN 3w, compared to SYN 5m and SYN 18m. In other words, in young synapses the isoform 201 (short 5′UTR) seems to be preferred (Figure 6J). In agreement with this result, the amplicon spanning the junction 1–2 is less expressed in SYN 3w, compared to SYN 5m and SYN 18m (Figure 6O'). The isoform 201, which is predominant in young animals, is characterized by a much smaller 5′UTR. Although this isoform is already annotated, its biological function has not been studied yet. The presence of a short 5′UTR can have a variety of implications for the transcript localization, stability, and translation rate, and that, on the other hand, could allow for an age-dependent global regulation of synaptic translation.

3 | Discussion

Synaptic function and plasticity critically depend on transcript differential localization and local translational control. Several seminal studies analyzed the synaptic transcriptome and the mechanisms regulating its local translation. All these previous studies investigated young or adult animals, and the topic of translational remodeling and transcript trafficking during aging remained unexplored. Our results show that during adulthood, the regulation of proteins and transcripts at the synapse is tightly coordinated with molecular changes occurring in neuronal cell bodies. However, during aging, this coupling is progressively disrupted, leading to both protein–transcript uncoupling and soma–synapse uncoupling at multiple levels. This includes alterations in the localization and expression of proteins and transcripts, as well as synapse-specific changes in splicing patterns.

A loss of protein–transcript correlation is observed already in the transition between young- and adult-life stages. The reason underlying the loss of correlation between absolute levels of protein and transcripts can be multiple. One main factor relates to protein half-lives. Proteins with large half-lives accumulate even if the corresponding transcript decreases or is stable (Kelmer Sacramento et al. 2020). These changes cannot be regarded as regulations in common sense. Protein and transcript regulations are active processes, and our data show that age-dependent changes between young and adult stages are highly correlated, indicating that these processes remain coordinated in adult life despite the loss of correlation in absolute protein and transcript levels.

Aging is particularly associated with synapse-specific translational remodeling, with ribosomal protein-coding transcripts exhibiting striking changes. In young synapses, these transcripts are enriched but translationally repressed, suggesting a tightly regulated mechanism controlling ribosomal protein production. In contrast, during aging, these transcripts become downregulated at the synapse while simultaneously displaying increased association with ribosomes. The presence of higher levels of ribosomal proteins, despite a reduction of the corresponding transcripts, delineates a purely posttranscriptional mechanism driven by an increase in translational efficiency (TE) of transcripts coding for ribosomal proteins specifically in the aging synaptosomes. This translational remodeling is in stark contrast with a remodeling in the opposite direction in TH, where ribosomal proteins decrease as a result of decreased TE. Loss of ribosomal proteins appears as a general phenomenon across a variety of mouse organs (Yu et al. 2020), and a decline in protein synthesis rate is generally associated with aging, representing an early event in neurodegenerative diseases (Halliday et al. 2017) and is thought to contribute to impaired synaptic function and cognitive deficits observed in physiological aging (Kim and Pickering 2023). Several studies have consistently reported enrichment for transcripts coding for ribosomal proteins and translational machinery in general at the synaptic level (Fusco et al. 2021; Seo et al. 2022), and local protein synthesis is a key mechanism to sustain synaptic maintenance and plasticity (Monday et al. 2022). These transcripts are under strict translational control; their translation is normally repressed (hence the corresponding protein levels are low), but their translation is activated by electrical stimulation (Shigeoka et al. 2019). The translational remodeling observed at the synapse may represent an

adaptive mechanism to maintain synaptic function by ensuring adequate protein synthesis during aging. Alternatively, it could reflect the loss of active translational repression that ensures activity-dependent control of protein synthesis in young animals. In either case, increased synthesis of translational machinery must cause a global translational remodeling affecting synaptic protein synthesis.

In our study, we have not investigated posttranslational modifications, such as phosphorylation and ubiquitination. These modifications are well known to have a profound influence on synaptic function and synaptic plasticity. Of particular note, a recent study demonstrated prominent age-dependent ubiquitination of the SNARE complex and loss of ubiquitination of postsynaptic proteins in the mouse brain (Marino et al. 2025). So, it is likely that post translational modification will also influence synaptic function in the aging brain providing an additional level of regulation with respect to those we analyzed in the present study.

4 | Materials and Methods

4.1 | Mouse Maintenance

Tissue from wild-type C57BL/6 mice was obtained from the Leibniz Institute on Aging, Fritz Lipmann Institute Jena, and from Janvier facility. Mice were housed in standard cages and fed standard lab chow and water ad libitum. Euthanasia was carried out by cervical dislocation in accordance with the European Council Directive of 22 September 2010 (2010/63/EU). The scientific purposes of the experiments were approved by the local authorities and supervised by the local veterinary (Anzeige N. O_AC_04, O_AC_08, O_AC_10, and O_AC_23–27).

4.2 | Synaptosome Preparation and Validation

Synaptosomes were extracted from cerebral cortices of 3-week-, 5-month- and 18/19-month-old mice as previously described (Gray and Whittaker 1962; Moczulska et al. 2014). Briefly, the cortex was dissected and transferred to ice-cold synaptosomal buffer (10 mM HEPES, 1 mM EDTA, 2 mM EGTA, 0.5 mM DTT, 0.32 M sucrose, pH 7) containing protein inhibitors (1 tablet/10 mL, Roche). Samples were homogenized using a pestle (Sigma-Aldrich) with 12 strokes on ice. The homogenate was then centrifuged for 10 min at 1000 *g* at 4°C and the supernatant was centrifuged again for 40 min at 10,000 *g* at 4°C. The obtained pellet, that contains the synaptosomes, was then resuspended in ice-cold synaptosomal buffer and layered over a discontinuous sucrose gradient (0.8 M/1 M/1.18 M sucrose). The samples were then centrifuged for 2 h at 50,512 *g* at 4°C (Beckman Coulter Optima XPN-80 ultracentrifuge). The interface between 1 and 1.18 M was withdrawn (synaptosome sample) and stored at −80°C. Aliquots were taken after the homogenization (total homogenate samples), after the first centrifugation (cytosolic fraction samples) and after the resuspension of the pellet containing the synaptosomes (raw synaptosomes samples).

Synaptosome samples were processed for RNA extraction according to (Smalheiser et al. 2014), and RNA was then extracted from the appositely prepared synaptosome samples and from TH samples through acidic phenol–chloroform extraction according to (Chomczynski 1993). The synaptosomes were diluted in synaptosomal RNA buffer (50 mM Hepes, pH 7.5, 125 mM NaCl, 100 mM sucrose, 2 mM K acetate, 10 mM EDTA) containing protease inhibitors (1 tablet/10 mL, Roche, Cat. No. 11836170001), 160 U/mL Superase-In (Invitrogen, Cat. No. AM2694), 160 U/mL Rnase-OUT (Invitrogen, Cat. No. 10777019), quickly pelleted at 20,000 *g* for 20 min and rinsed twice in 4× volume of synaptosomal RNA buffer and spundown again 20,000 *g* for 20 min. They were then resuspended in 100 μL of synaptosomal RNA buffer, and RNA was extracted with standard Trizol protocol (Chomczynski and Sacchi 1987) using Qiazol lysis reagent (Qiagen Cat. No. 79306).

Validation of the synaptosomes enrichment procedure was performed through Western Blot and qPCR. In the former case, the enrichment of NMDAR2B (Abcam, Cat. No. ab65783) and the depletion of Histone H3 (Abcam, Cat. No. ab1791) were evaluated and compared to α-Tubulin (Sigma-Aldrich, Cat. No. T9026) levels. In the latter case, complementary DNA (cDNA) was produced using the SuperScript IV Reverse Transcriptase (ThermoScientific, Cat. No. 18090010), following the manufacturer's instructions. cDNA was obtained from 100 ng of total brain extract RNA and total synaptosomal RNA and was used for qPCR using SYBR Green PCR Master Mix (Qiagen, Cat. No. 208052) according to the manufacturer's instructions. A two-step program was run on a Biorad C1000 Touch cycler (Biorad) using 60° as the annealing and extension temperature and generating a melting curve. The expression values of each synaptic and noncoding gene were normalized on H3F3B, coding for the histonic protein 3 B (for details about the primers used see table below).

For the validation of ribosomal proteins increasing with aging, the enrichments of RPL10A (Abcam, Cat. No. ab226381), RPS6 (Cell Signaling, Cat. No. #2217), RPL7 (Bethyl, Cat. No. A300-741A), and RPL15 (LS Bio, Cat. No. LS-C162700) were evaluated and compared to α-Tubulin (Sigma-Aldrich, Cat. No. T9026) levels, both in TH and SYN. The validation of the depletion of RNAs coding for ribosomal proteins from SYN by qPCR was done as described above. The expression values of each ribosomal gene were normalized on Ldhb, a transcript whose expression is stable in the two fractions analyzed across all time points (for details about the primers used see table below).

The validation of the differentially spliced regions by qPCR was done normalizing each junction with a reference exon as described in the text and didascalies (for details about the primers used see table below).

Target gene	Forward primer	Reverse primer	Amplicon size
Camk2a (ENSMUSG00000024617)	acctgcacccgattcacag (Exon 1)	tggcagcatactcctgacca (Exon 2)	112 bp
Dlg4 (ENSMUSG00000020886)	accagaagagtatagccgattcg (Exon 10–11)	ggtcttgtcgtagtcaaacagg (Exon 12)	148 bp
Gria1 (ENSMUSG00000020524)	gctttgtcacaactcacgga (Exon 2)	cctttggagaactgggaaca (Exon 3)	110 bp
Arc (ENSMUSG00000022602)	ggtgagctgaagccacaaat (Exon 1)	gctgagctctgctcttcttca (Exon 2)	101 bp
H3f3b (ENSMUSG00000016559)	aagcagaccgctaggaagtc (Exon 4)	ggtaacgacggatctctctcag (Exon 5)	154 bp
Gm34838 (ENSMUSG00000110028)	ggctcctctatgttggaatatg (Exon 2)	tgcttccaaagtccttcagt (Exon 3)	119 bp
Gm10925 (ENSMUSG00000100862)	aatcctattcccatcctcaa (Exon1)	agggaaacaattattagggttc (Exon 1)	141 bp
Gm13340 (ENSMUSG00000083563)	aataccaataataatcggaggc (Exon 1)	agactgttcatcctgttcctg (Exon 1)	176 bp
Ldhb-201 (ENSMUSG00000030246)	ccgaacaacaagatcactgta (Exon 2)	gagcttgtcttccaacacat (Exon 3)	120 bp
Rpl10a-201 (ENSMUSG00000037805)	gcactgtgatgaagccaagg (Exon 4)	tcagagactcagaggccaaa (Exon 5)	134 bp
Rpl15-202 (ENSMUSG00000012405)	cggcctgataaagctcga (Exon 2)	gccgtaagttgcacccttag (Exon 3)	117 bp
Rpl26-201 (ENSMUSG00000060938)	tgacgaagttcaggttgttcg (exon junction 2–3)	cttctctcgctggactcgtt (Exon 3)	112 bp
Rpl7-201 (ENSMUSG00000043716)	tccttgattgctcggtctct (Exon 5)	tgaagggccacaggaagtta (Exon 6)	118 bp
Rps13-201 (ENSMUSG00000090862)	tgacgacgtgaaggaacaga (Exon 3)	gtcacaaaacggacctggg (Exon 4)	111 bp
Rps6-201 (ENSMUST00000102814)	agaagatgatgtccgccagt (Exon 4)	cgaggagtaacaagtcgctg (Exon 5)	102 bp
Eif2b3–203 (ENSMUST00000106448)	tggcttgtcagccagagg (Exon 1)	gggaatgctggaagtcaagt (Exon 2)	146 bp
Eif2b3-203 (ENSMUST00000106448)	gggatctcggatgacagact (Exon 2)	cttcaaatccaacacgctca (Exon 2)	113 bp
Birc2-204 (ENSMUST00000190341)	gtcctgcatcctttggtgat (Exon 4b)	caccaggctcctactgaagc (Exon 5)	145 bp
Birc2-204 (ENSMUST00000190341)	atgagcacgcctgtggtta (Exon 5)	cggtcctgtagttctcaccag (Exon 5)	109 bp
Birc2-204 (ENSMUST00000190341)	ttcagacaccccaggagaag (Exon 4)	caccaggctcctactgaagc (Exon 5)	Variable
Bcas1-201 (ENSMUST00000013667)	agacagcggcaaggagaag (Exon 8)	ctctgcacctgtggaaagtg (Exon 9)	100 bp
Bcas1-201 (ENSMUST00000013667)	aacttcacaccccaggagac (Exon 8)	aaacaactttcccagcggta (Exon 8)	147 bp
Bcas1-201 (ENSMUST00000013667)	gctgggaaagttgttttgga (Exon 8)	gtccttcgaggaggaggtct (Exon 12)	Variable

(Continues)

Target gene	Forward primer	Reverse primer	Amplicon size
Nfasc-202 (ENSMUST00000094569)	agaccaagttctctgtgcag (Exon 23)	tgcagttggagtagcttca (Exon 24)	137 bp
Nfasc-202 (ENSMUST00000094569)	tggtggaaaacttctctccca (Exon 23)	cttcatttggaggtgctggg (Exon 23)	147 bp
Nfasc-202 (ENSMUST00000094569)	ccccagcacctccaaatgaa (Exon 23)	tgatgggaactgttgtggct (Exon 25)	Variable
Nfasc-203 (ENSMUST00000163770)	tccttaagaaaccaccctgaca (Exon 8)	attccagcagcaggtccat (Exon 9)	127 bp
Nfasc-203 (ENSMUST00000163770)	gaggagttgcagaaagaacgc (Exon 9)	attccagcagcaggtccat (Exon 9)	93 bp
Nfasc-203 (ENSMUST00000163770)	agaaccccttcaccctcaag (Exon 7)	attccagcagcaggtccat (Exon 9)	Variable
Nfasc-201 (ENSMUST00000043189)	cgagtccaggctgaaaatgac (Exon 19)	gttccactgaaggctgatgg (Exon 20)	144 bp
Nfasc-201 (ENSMUST00000043189)	ccccaacctacgctacattg (Exon 19)	tcattttcagcctggactcg (Exon 19)	144 bp
Nfasc-201 (ENSMUST00000043189)	cgagtccaggctgaaaatgac (Exon 19)	ggtcccactccaggttgatg (Exon 22)	Variable
Ankfy1-206 (ENSMUST00000155998)	atcgttcggtctggggtt (Exon 23)	ttcatagcagttggagccg (Exon 24)	150 bp
Ankfy1-206 (ENSMUST00000155998)	gaatgccaacttgtgccgt (Exon 23)	ctgcttagtggcaacctggtag (Exon 23)	103 bp
Ankfy1-206 (ENSMUST00000155998)	ctaccaggttgccactaagc (Exon 23)	caggcttgttcaggtcaaact (Exon 25)	Variable
Snrnp70-204 (ENSMUST00000209993)	gctccccttacaacacctca (Exon 6)	ctccagcccttcacagtcc (Exon 7)	115 bp
Snrnp70-204 (ENSMUST00000209993)	agatagatggcaggagggtc (Exon 7)	tattcacatctgccccacct (Exon 8)	120 bp
Snrnp70-204 (ENSMUST00000209993)	taaacgctctggaaaacccc (Exon 5)	gaccctcctgccatctatct (Exon 7)	Variable
Rsrc2-210 (ENSMUST00000182489)	ctgttgagtgcgggcaag (Exon 1)	tggcacagaggtacagcaaa (Exon 2)	115 bp
Rsrc2-210 (ENSMUST00000182489)	gccctagaaaagacatcaccg (Exon 3)	cttgaccttgacctcgacct (Exon 3)	110 bp
Rsrc2-210 (ENSMUST00000182489)	ctgttgagtgcgggcaag (Exon 1)	cggtgatgtcttttctagggc (Exon 3)	Variable

4.3 | Immunofluorescence of Isolated Synaptosomes

Isolated synaptosomes were plated on glass coverslips (10 μg per coverslip) by centrifugation at 4000 rpm for 40 min at 4°C. Fixation was performed with 4% PFA in PBS (137 mM NaCl, 2.7 mM KCl, 10 mM Na_2HPO_4, 2 mM KH_2PO_4) at pH 7.5 for 10 min on ice followed by 35 min at room temperature. Coverslips were then washed briefly with PBS 2–3 times, and PFA was quenched with 100 mM NH_4Cl for 25 min. They were then permeabilized and blocked in staining solution (PBS + 4% donkey serum, 2% BSA, and 0.1% Triton-X-100) for 30 min. Primary and secondary antibodies were applied in staining solution for 2 h and 1 h, respectively; washing between primary and secondary antibody incubation was 3 × 5 min, with PBS. After the secondary antibody incubation, cells were sequentially washed 3 × 5 min with PBS + 3 × 5 min high-salt PBS (PBS + 350 mM NaCl), and 3 × 5 min PBS to increase the stringency of the antibody staining. Finally, synaptosomes were embedded in ProLong glass antifade medium (Invitrogen, Cat. No. P36982) for imaging. The primary antibodies used were the following: Synaptophysin (Synaptic Systems, Cat. No. 101004),

RPL7 (Bethyl, Cat. No. A300-741A), and rRNA (Y10b) (Novus biologicals, Cat. No. NB100-662). Coverslips were imaged with an AiryScan microscope (Zeiss). For unbiased, systematic processing of the images, an ImageJ macro was written to perform the analysis blind to age by keeping all parameters constant throughout. The synaptophysin channel (presynaptic vesicle pool marker) was used to identify the regions to analyze, and a constant threshold was applied and maintained for all images (to avoid bias across conditions). Individual synapses were selected and measured using the ImageJ particle analysis tool. Regions of interest (ROIs) were defined, added to the ROI manager, and automatically measured for the other two acquired channels (rRNA and RPL7). Fluorescence intensities and sizes were automatically saved to CSV files and further processed in R and GraphPad for statistical treatment.

4.4 | Isolation of Ribosome-Associated RNAs From TH and SYN

Ribosome-associated RNAs were purified using a sucrose cushion as previously described (Fusco et al. 2021). Briefly, pelleted synaptosomes or 50 μL of TH were lysed with 1 mL ribosome lysis buffer (20 mM Tris pH 7.4, 150 mM NaCl, 5 mM $MgCl_2$, 24 U/mL TurboDNase, 100 μg/mL cycloheximide, 1% Triton-X-100, 1 mM DTT, RNasin(R) Plus RNase inhibitor 200 U/mL and 1× cOmplete EDTA-free protease inhibitor). TH samples were then homogenized with a syringe and a 0.4×20 mm needle on ice and centrifuged for 10 min at 10,000 *g* at 4°C. TH and SYN were then loaded on 3 mL sucrose solution (34% sucrose, 20 mM Tris pH 7.4, 150 mM NaCl, 5 mM $MgCl_2$, 1 mM DTT, 100 μg/mL cycloheximide) in a thickwall ultraclear tube (Beckman, 344062) and centrifuged for 40 min at 4°C at 55,000 rpm (367,600×*g*) with a SW60 rotor. Ribosome-containing pellet was directly collected in Qiazol (Qiagen Cat. No. 79306) and processed for RNA extraction.

4.5 | RNA Sequencing

RNA Sequencing was performed on the TH and SYN samples. Prior to that, RNA integrity (RIN Score) and RNA concentration were estimated using the Bioanalyzer 2100 (Agilent) and the RNA 6000 Pico Kit and RNA 6000 Nano Kit for SYN and TH samples, respectively. Sequencing of RNA samples was performed using Illumina's next-generation sequencing (Bentley et al. 2008). In detail, total RNA was quantified and quality checked using the Agilent 2100 Bioanalyzer in combination with an RNA 6000 Pico assay (both Agilent Technologies). Libraries were prepared from 10 ng of input material (total RNA) using the SMARTer Stranded Total RNA-Seq Kit—Pico Input Mammalian (Takara, Cat. No. 635006), following the manufacturer's instructions. Quantification and quality checking of libraries were done using an Agilent 2100 Bioanalyzer instrument and a DNA 7500 kit (Agilent Technologies). Libraries were pooled and sequenced using a HiSeq 2500 system run in Rapid v2/51 cycle/single-end mode. Sequence information was converted to FASTQ format using bcl2FastQ v2.19.0.316. Per sample, the reads were mapped to the *Mus musculus* genome GRCm38 and respective annotation Release 85 [PMID: 29155950] using tophat2 v2.1 [PMID: 23618408] (parameters: --no-coverage-search --no-convert-bam --no-novel-juncs --no-novel-indels -T). Reads per gene were counted using featureCounts v1.5 [PMID: 24227677] (parameters: -s 0). Read counts were introduced into the statistical environment R in order to calculate RPMs (reads per million mappable reads) and RPKMs (reads per kilobase and million mappable reads). For the calculation of RPKMs, lengths of transcripts were taken from featureCounts output.

For the RNAs obtained by sucrose cushion, total RNA was quantified and quality checked using Tapestation 4200 instrument in combination with RNA ScreenTape (both Agilent Technologies). Libraries were prepared from 30 to 150 ng of input material (total RNA) using NEBNext Ultra II Directional RNA Library Preparation Kit in combination with NEBNext rRNA Depletion Kit v2 (Human/Mouse/Rat) and NEBNext Multiplex Oligos for Illumina (Unique Dual Index UMI Adaptors RNA) following the manufacturer's instructions (New England Biolabs). Quantification and quality checked of libraries was done using an Agilent 4200 Tapestation instrument and a D1000 ScreenTape (Agilent Technologies). Libraries were pooled and sequenced in two NovaSeq6000 S1 100 cycle runs. System run in 101 cycle/single-end/standard loading workflow mode. Sequence information was converted to FASTQ format using bcl2fastq v2.20.0.422. Sequencing finished with an average of 39.6 million reads per sample. Mapping was done as described above.

For the alternative splicing analysis, a paired-end 2×150 bp sequencing was performed using the Illumina HiSeq2500 System and the HiSeq Rapid SBS Kit v2. Sequence information was extracted in FASTQ format using Illumina's bcl2FastQ 2.20.0.422, and processed raw reads were finally mapped to the Genome Reference Consortium Mouse Build 38 patch release 6 (GRCm38.p6) using Segemehl 0.3.4 in split-read mode (Hoffmann et al. 2009), obtaining SAM files. Using SAMtools 1.7 (Li et al. 2009) sorted BAM files and BAI files were generated. Raw counts were obtained using the featureCounts function 1.6.0 of the Subread package (Liao et al. 2014) (-p and --minOverlap 10 -s 1 -t exon -g gene_id).

4.6 | Sample Preparation for Mass Spectrometry (MS)

Samples were brought to the same sample volume (125 μL) with MilliQ water, then a 2× lysis buffer was added in equal volume, to yield the samples in 250 μL volume containing 1% SDS, 100 mM HEPES pH 8.5, and 50 mM DTT. 4× acetone volume was added for protein precipitation. A maximum g of 3220 could be used during all steps to obtain protein pellets.

Samples were sonicated with 10 cycles (60 s ON, 30 s OFF) using the high energy mode in a Bioruptor (Diagenode) at 20°C. The samples were then boiled (95°C, 10 min) before being subjected to another 10 cycles in the Bioruptor. Iodoacetamide (IAA) was added to a final concentration of 15 mM, and the samples incubated in the dark for 30 min at room temperature. Proteins were precipitated with 4 volumes equivalent of ice-cold acetone overnight at −20°C. The following day, samples were centrifuged at 4°C, 14,000 rpm for 30 min (Eppendorf 5804R benchtop centrifuge), then the acetone supernatant was carefully removed. Protein pellets were washed twice with ice cold 80% acetone/20% water (500 μL each time) and centrifuged at 4°C, 14,000 rpm for 10 min each wash.

After the last wash, the acetone/water was removed, and the pellets were allowed to air dry at room temperature.

Protein pellets were then resuspended in digestion buffer (3 M Urea in 100 mM HEPES, pH 8) at a concentration of 1 μg/μL and sonicated using a Bioruptor for three cycles (60 s ON/30 s OFF). Proteins were digested with Lys-C protease (Wako, Cat. No. 125-05061) at a 1:100 enzyme: protein ratio (4 h, 37°C, with shaking 1000 rpm), then diluted with milliQ water (for a final concentration of 1.5 M Urea) and further digested with Trypsin (Promega, Cat. No. V5280) at a 1:100 enzyme: protein ratio (overnight, 37°C, 650 rpm). Samples were acidified the following day by the addition of 10% Trifluoracetic Acid (TFA) and then desalted with Waters Oasis HLB μElution Plate 30 μm (Cat. No. 186001828BA) in the presence of a slow vacuum. In this process, the columns were conditioned with 3 × 100 μL solvent B (80% acetonitrile; 0.05% formic acid) and equilibrated with 3 × 100 μL solvent A (0.05% formic acid in milliQ water). The samples were loaded, washed three times with 100 μL solvent A, and then eluted into PCR tubes with 50 μL solvent B. The eluates were dried down with the speed vacuum centrifuge and dissolved at a concentration of 1 μg/μL in 5% acetonitrile, 95% milliQ water, with 0.1% formic acid prior to analysis by LC–MS/MS.

4.7 | LC–MS/MS for Data Independent Analysis (DIA)

Peptides were separated using the nanoAcquity UPLC M-Class system (Waters) fitted with a trapping (nanoAcquity Symmetry C18, 5 μm, 180 μm × 20 mm) and an analytical column (nanoAcquity BEH C18, 1.7 μm, 75 μm × 250 mm). The outlet of the analytical column was coupled directly to Q-Exactive HFX (Thermo Fisher Scientific) using the Proxeon nanospray source. Solvent A was water, 0.1% formic acid, and solvent B was acetonitrile, 0.1% formic acid. The samples (approx. 1 μg) were loaded with a constant flow of solvent A at 5 μL/min onto the trapping column. Trapping time was 6 min. Peptides were eluted via the analytical column with a constant flow of 0.3 μL/min. During the elution step, the percentage of solvent B increased in a nonlinear fashion from 0% to 40% in 60 min. Total runtime was 75 min, including clean-up and column re-equilibration. The peptides were introduced into the mass spectrometer via a Pico-Tip Emitter 360 μm OD × 20 μm ID; 10 μm tip (New Objective), and a spray voltage of 2.2 kV was applied. The capillary temperature was set at 300°C. The RF ion funnel was set to 40%. Data from the TH samples were first acquired in DDA mode to contribute to a sample-specific spectral library. The conditions were as follows: full scan MS spectra with mass range 350–1650 m/z were acquired in profile mode in the Orbitrap with a resolution of 60,000. The filling time was set at a maximum of 20 ms with a limitation of 1×10^6 ions. The "Top N" method was employed to take the 15 most intense precursor ions (with an intensity threshold of 4×10^4) from the full scan MS for fragmentation (using HCD normalized collision energy, 31%) and quadrupole isolation (1.6 Da window) and measurement in the Orbitrap (resolution 15,000, fixed first mass 120 m/z). The peptide match "preferred" option was selected, and the fragmentation was performed after accumulation of 2×10^5 ions or after a filling time of 25 ms for each precursor ion (whichever occurred first). MS/MS data were acquired in profile mode. Only multiply charged (2+ to 5+) precursor ions were selected for MS/MS. Dynamic exclusion was employed with a maximum retention period of 30 s and a relative mass window of 10 ppm. Isotopes were excluded. In order to improve the mass accuracy, internal lock mass correction using a background ion (m/z 445.12003) was applied. For data acquisition and processing of the raw data, Xcalibur 4.0 (Thermo Scientific) and Tune version 2.9 were employed. For the DIA data acquisition, the same gradient conditions were applied to the LC as for the DDA, and the MS conditions were varied as described: full scan MS spectra with mass range 350–1650 m/z were acquired in profile mode in the Orbitrap with a resolution of 120,000. The default charge state was set to 3+. The filling time was set at a maximum of 60 ms with a limitation of 3×10^6 ions. DIA scans were acquired with 34 mass window segments of differing widths across the MS1 mass range. HCD fragmentation (stepped normalized collision energy; 25.5, 27, 30%) was applied, and MS/MS spectra were acquired with a resolution of 30,000 with a fixed first mass of 200 m/z after accumulation of 3×10^6 ions or after a filling time of 47 ms (whichever occurred first). Data were acquired in profile mode. All samples (both TH and SYN) had data acquired in DIA mode.

4.8 | Parallel Reaction Monitoring (PRM) for Ribosomal Peptides

Six peptides for quantification of ribosomal proteins (table below) were selected from previous publications and their isotopically labeled version (heavy arginine (U-13C6; U-15N4) or lysine (U-13C6; U-15N2) at the C-term was added) synthesized by JPT Peptide Technologies GmbH (Berlin, Germany) as SpikeTides TQL quality grade. Lyophilized peptides were delivered as 10 dried 1 nmol aliquots on a 96-well plate and reconstituted in 20% (v/v) acetonitrile, 0.1% (v/v) formic acid with a final concentration of 0.05 nmol/μL and further pooled together in a ratio 1:1. Peptides were resuspended at a final concentration of 2.5 fmol/μL and 1 μL was analyzed by both DDA and DIA LC–MS/MS and used for assay generation using Spectrodive v.12.0.4 (Biognosys AG, Schlieren, Switzerland).

Peptides were separated using a nanoAcquity UPLC M-Class system (Waters, Milfors, MA, USA) with trapping (nanoAcquity Symmetry C18, 5 μm, 180 μm × 20 mm) and an analytical column (nanoE MZ HSS C18 T3 1.8 μ, 75 μm × 250 mm). The outlet of the analytical column was coupled directly to an Orbitrap Fusion Lumos (Thermo Fisher Scientific, Waltham, MA, USA) using the Proxeon nanospray source. Solvent A was water, 0.1% (v/v) formic acid and solvent B was acetonitrile, 0.1% (v/v) formic acid. Peptides were eluted via the analytical column with a constant flow of 0.3 μL/min. During the elution step, the percentage of solvent B increased nonlinearly from 0% to 25% in 15 min, then 25%–50% in 1 min. During the elution step, the percentage of solvent B increased in a nonlinear fashion from 0% to 40% in 40 min. Total runtime was 60 min, including clean-up and column re-equilibration. PRM acquisition was performed in an unscheduled fashion for the duration of the entire gradient using the "tMSn" mode with the following settings: resolution 120,000 FWHM, AGC target 3×10^6, maximum injection time (IT) 750 ms, isolation window 0.5 m/z. For each cycle, a "full MS" scan was acquired with the following settings: resolution

120,000 FWHM, AGC target 3×10^6, maximum injection time (IT) 10 ms, scan range 350–1650 m/z. Quantification was performed using spike-in approach. Thereby, the summed height of all the identified transitions was used to estimate the quantity of each peptide. Afterward, the ratio between endogenous (light) and reference (heavy) peptides was calculated and normalized to the extracted base peak chromatogram area coming from MS1 measurement.

Target gene	Peptide sequence
RPL15	_SLQSVAEER_
RPL15	_QGYVIYR_
RPL10a	_ILGPGLNK_
RPL7	_VATVPGTLK_
RPS6	_LIEVDDER_
RPS6	_KLFNLSKEDDVR_

4.9 | Data Analysis for DIA Data

For library creation, the DDA data were searched using Pulsar (v. 1.0.15764.0.27599) (Biognosys AG, Switzerland). The data were searched against a species-specific (*Mus musculus*) Swissprot database with a list of common contaminants appended, as well as the HRM peptide sequences. The data were searched with the following modifications: Carbamidomethyl (C) (Fixed) and Oxidation (M)/Acetyl (Protein N-term) (Variable). A maximum of 1 missed cleavage was allowed, and the identifications were filtered to satisfy an FDR of 1% on the peptide and protein level.

Also for library creation, the DIA data were searched using Pulsar (v.1.0.15764.0.27599). The data were searched against a species-specific (*M. musculus*) Uniprot database with a list of common contaminants appended, as well as the HRM peptide sequences. The data were searched with the following modifications: Carbamidomethyl (C) (Fixed) and Oxidation (M)/Acetyl (Protein N-term) (Variable). DpD (DDA plus DIA) libraries were then created by combining the spectral library created from the output of the DDA runs with the searched libraries using Spectronaut (v. 11; Biognosys AG, Switzerland) (Bruderer et al. 2015). This library contained 78.629 precursors, corresponding to 4.216 protein groups using Spectronaut protein inference. DIA data were then uploaded and searched against this spectral library. Relative quantification was performed in Spectronaut for each pairwise comparison using the replicate samples from each condition. The data (candidate table) and data reports were then exported to Excel, and further data analyses and visualization were performed with R-studio (version 0.99.902) using in-house pipelines and scripts.

4.10 | Data Analysis

All the analyses were performed using R-Studio 1.1.456 (Leemans et al. 2009). Starting from the raw counts, normalized counts and $\log_2$ fold changes were estimated using DESeq2 1.22.2 (Love et al. 2014). To combine transcriptomic and proteomic data, p values for differential expression at the protein and transcript level are combined in a meta-analysis (Fisher's method) (Lury 1972). Fisher's method combines extreme value probabilities from each test, commonly known as "p values," into one test statistic (χ^2) using the formula:

$$X_{2k}^2 \sim -2 \sum_{i=1}^{k} \ln(p_i)$$

where p_i is the p value for the ith hypothesis test.

The visualization of the sample's similarity through Gene Enrichment has been evaluated by performing overrepresentation analysis (ORA) using the WebGestalt website (http://webgestalt.org/) (Liao et al. 2019). This website uses affinity propagation to cluster similar gene sets; it identifies the most enriched GO categories in a given dataset and provides the FDR-corrected p value of the enrichment. The categories of the GO database (Ashburner et al. 2000; The Gene Ontology consortium 2017) that contain at least five genes were considered, and the p values have been corrected for multiple comparisons through the FDR method described in (Benjamini and Hochberg 1995). Visualization of Gene Enrichment was achieved using ReviGO software (http://revigo.irb.hr/). ReviGO allows obtaining a flexible reduction in size for large user-supplied lists of overlapping GO categories and visualizes the remaining GO terms in a two-dimensional space that reflects the terms' semantic interrelations.

Classification of genes as coding or noncoding was done using Ensembl BioMart (https://www.ensembl.org/biomart/) annotation version GRCm38.p6.

Principal component analysis and heatmap representation of their hierarchical clustering has been performed using DESeq2's internal functions and the packages ComplexHeatmap 2.0.0, pcaMethods 1.76.0 and ggpubr 0.2. Density plots have been drawn using the packages ggplot2 3.1.1 and ggpubr 0.2.

Generally applicable gene set enrichment for pathway analysis (GAGE) was performed using gage 2.34.0 and GO.db 3.8 packages (Luo et al. 2009). GAGE is a published method for gene set (enrichment or GSEA) or pathway analysis. To test whether a gene set is significantly correlated with a phenotype or an experimental condition, the fold changes of gene expression levels in the experimental condition (or phenotype) are compared to a control condition. Then, a two-sample t-test is applied to verify whether the mean fold changes of a target gene set are significantly different from that of the background set (the whole gene set of the microarray).

In ribosome profiling experiments, Translational Efficiency (TE) is generally defined as the ratio between the Ribosome Protected Fragments (RPFs) and mRNA counts. Since we were dealing with whole transcripts associated with ribosomes, we calculated SYN TE as the ratio between ribosome-associated transcripts (SC) in SYN and TH. When examining a single compartment (either SYN or TH), we calculated TE as the ratio

between ribosome-associated transcripts (SC) and all transcripts in that compartment (input).

4.11 | Identification of Differentially Expressed Junctions (DEJs)

DEJs were identified using the software DIEGO (Doose et al. 2018) and LeafCutter (Li et al. 2018). Gene models and the coverage at genomic intervals of interest were visualized using the software IGV 2.5.2 (Robinson et al. 2011; Thorvaldsdóttir et al. 2013) and the R packages rtracklayer 1.44.0 (Lawrence et al. 2009), GenomicRanges 1.36.0, and GenomicFeatures 1.36.1 (Lawrence et al. 2013) and ggbio 1.32.0 (Yin et al. 2012).

Author Contributions

C.C., M.U., S.H., and A.C. project design. C.C., M.U., W.D., K.J., M.G., K.R., and M.G. data production. C.C., M.U., E.F., and A.C. data analysis. C.C., M.U., E.F., S.H., and A.C. data interpretation. S.H. and A.C. supervision and coordination. C.C., M.U. and A.C. drafting the manuscript. All authors contributed to the final version of the manuscript.

Acknowledgments

The Core Facilities and Services CF Next-generation sequencing (Cornelia Luge and Ivonne Goerlich), CF Life science computing, and CF proteomics of the FLI are gratefully acknowledged for their technological support. Dr. Mario Baumgart is gratefully acknowledged for the help with internal animal permissions. We thank Sabine Matz for the excellent technical support. A.C. is supported by the German Research Council (DFG, award nos. CE 257/9-1 and CE 257/9-2) and by Next Generation EU (PNRR), "Tuscany Health Ecosystem," THE project code ECS 00000017. Open Access funding enabled and organized by Projekt DEAL.

Conflicts of Interest

The authors declare no conflicts of interest.

Data Availability Statement

The RNA-seq datasets here presented are available on GEO: GSE281456, GSE281455, and GSE146636. The proteomics dataset is available on MassIVE at the following link: https://massive.ucsd.edu/ProteoSAFe/private-dataset.jsp?task=b2cf624f9229489eb9f47b22b7e9244f.

References

Ahmari, S. E., J. A. Buchanan, and S. J. Smith. 2000. "Assembly of Presynaptic Active Zones From Cytoplasmic Transport Packets." *Nature Neuroscience* 3, no. 5: 445–451. https://doi.org/10.1038/74814.

Anders, S., A. Reyes, and W. Huber. 2012. "Detecting Differential Usage of Exons From RNA-Seq Data." *Genome Research* 22, no. 10: 2008–2017. https://doi.org/10.1101/gr.133744.111.

Ashburner, M., C. A. Ball, J. A. Blake, et al. 2000. "Gene Ontology: Tool for the Unification of Biology." *Nature Genetics* 25, no. 1: 25–29. https://doi.org/10.1038/75556.

Benjamini, Y., and Y. Hochberg. 1995. "Controlling the False Discovery Rate: A Practical and Powerful Approach to Multiple Testing." *Journal of the Royal Statistical Society, Series B: Statistical Methodology* 57, no. 1: 289–300. https://doi.org/10.1111/j.2517-6161.1995.tb02031.x.

Bentley, D. R., S. Balasubramanian, H. P. Swerdlow, et al. 2008. "Accurate Whole Human Genome Sequencing Using Reversible Terminator Chemistry." *Nature* 456, no. 7218: 53–59. https://doi.org/10.1038/nature07517.

Bruderer, R., O. M. Bernhardt, T. Gandhi, et al. 2015. "Extending the Limits of Quantitative Proteome Profiling With Data-Independent Acquisition and Application to Acetaminophen-Treated Three-Dimensional Liver Microtissues." *Molecular & Cellular Proteomics* 14, no. 5: 1400–1410. https://doi.org/10.1074/mcp.M114.044305. Epub 2015 Feb 27.

Buckner, R. L. 2004. "Memory and Executive Function in Aging and AD: Multiple Factors That Cause Decline and Reserve Factors That Compensate." *Neuron* 44, no. 1: 195–208. https://doi.org/10.1016/j.neuron.2004.09.006.

Cagnetta, R., J. G. Flanagan, and N. Sonenberg. 2023. "Control of Selective mRNA Translation in Neuronal Subcellular Compartments in Health and Disease." *Journal of Neuroscience* 43, no. 44: 7247–7263. https://doi.org/10.1523/JNEUROSCI.2240-22.2023.

Chen, B. J., U. Ueberham, J. D. Mills, et al. 2017. "RNA Sequencing Reveals Pronounced Changes in the Noncoding Transcriptome of Aging Synaptosomes." *Neurobiology of Aging* 56: 67–77. https://doi.org/10.1016/j.neurobiolaging.2017.04.005.

Chomczynski, P. 1993. "A Reagent for the Single-Step Simultaneous Isolation of RNA, DNA and Proteins From Cell and Tissue Samples." *BioTechniques* 15, no. 3: 532–534.

Chomczynski, P., and N. Sacchi. 1987. "Single-Step Method of RNA Isolation by Acid Guanidinium Thiocyanate-Phenol-Chloroform Extraction." *Analytical Biochemistry* 162, no. 1: 156–159. https://doi.org/10.1016/0003-2697(87)90021-2.

Cioni, J. M., M. Koppers, and C. E. Holt. 2018. "Molecular Control of Local Translation in Axon Development and Maintenance." *Current Opinion in Neurobiology* 51: 86–94. https://doi.org/10.1016/j.conb.2018.02.025.

Daniel, J. A., C. S. Malladi, E. Kettle, A. McCluskey, and P. J. Robinson. 2012. "Analysis of Synaptic Vesicle Endocytosis in Synaptosomes by High-Content Screening." *Nature Protocols* 7, no. 8: 1439–1455. https://doi.org/10.1038/nprot.2012.070.

Dickstein, D. L., D. Kabaso, A. B. Rocher, J. I. Luebke, S. L. Wearne, and P. R. Hof. 2007. "Changes in the Structural Complexity of the Aged Brain." *Aging Cell* 6, no. 3: 275–284. https://doi.org/10.1111/j.1474-9726.2007.00289.x.

Dickstein, D. L., C. M. Weaver, J. I. Luebke, and P. R. Hof. 2013. "Dendritic Spine Changes Associated With Normal Aging." *Neuroscience* 251: 21–32. https://doi.org/10.1016/j.neuroscience.2012.09.077.

Dillman, A. A., E. Majounie, J. Ding, et al. 2017. "Transcriptomic Profiling of the Human Brain Reveals That Altered Synaptic Gene Expression Is Associated With Chronological Aging." *Scientific Reports* 7, no. 1: 16890. https://doi.org/10.1038/s41598-017-17322-0.

Doose, G., S. H. Bernhart, R. Wagener, and S. Hoffmann. 2018. "DIEGO: Detection of Differential Alternative Splicing Using Aitchison's Geometry." *Bioinformatics* 34, no. 6: 1066–1068. https://doi.org/10.1093/bioinformatics/btx690.

Du, H., L. Guo, and S. S. Yan. 2012. "Synaptic Mitochondrial Pathology in Alzheimer's Disease." *Antioxidants & Redox Signaling* 16, no. 12: 1467–1475. https://doi.org/10.1089/ars.2011.4277. Epub 2011 Dec 15.

Fard, M. K., F. Van der Meer, P. Sánchez, et al. 2017. "BCAS1 Expression Defines a Population of Early Myelinating Oligodendrocytes in Multiple Sclerosis Lesions." *Science Translational Medicine* 9, no. 419: 1–12. https://doi.org/10.1126/scitranslmed.aam7816.

Fjell, A. M., K. B. Walhovd, C. Fennema-Notestine, et al. 2009. "One-Year Brain Atrophy Evident in Healthy Aging." *Journal of Neuroscience* 29, no. 48: 15223–15231. https://doi.org/10.1523/JNEUROSCI.3252-09.2009.

Flurkey, K., J. M. Currer, and D. E. Harrison. 2007. "Mouse Models in Aging Research." In *The Mouse in Biomedical Research*, edited by J. G. Fox, S. W. Barthold, M. T. Davisson, C. E. Newcomer, F. W. Quimby, and A. L. Smith, vol. 3, 2nd ed., 637–672. Academic Press. https://doi.org/10.1016/B978-012369454-6/50074-1.

Fornasiero, E. F., S. Mandad, H. Wildhagen, et al. 2018. "Precisely Measured Protein Lifetimes in the Mouse Brain Reveal Differences Across Tissues and Subcellular Fractions." *Nature Communications* 9, no. 1: 4230. https://doi.org/10.1038/s41467-018-06519-0.

Fraia, D. D., A. Marino, J. H. Lee, et al. 2023. "A Comprehensive Atlas of the Aging Vertebrate Brain Reveals Signatures of Progressive Proteostasis Dysfunction." *BioRxiv*.

Fukushima, H., R. Maeda, R. Suzuki, et al. 2008. "Upregulation of Calcium/Calmodulin-Dependent Protein Kinase IV Improves Memory Formation and Rescues Memory Loss With Aging." *Journal of Neuroscience* 28, no. 40: 9910–9919. https://doi.org/10.1523/JNEUROSCI.2625-08.2008.

Fusco, C. M., K. Desch, A. R. Dörrbaum, et al. 2021. "Neuronal Ribosomes Exhibit Dynamic and Context-Dependent Exchange of Ribosomal Proteins." *Nature Communications* 12, no. 1: 6127. https://doi.org/10.1038/s41467-021-26365-x.

Garcia-Sanz, A., A. Badia, and M. V. Clos. 2001. "Superfusion of Synaptosomes to Study Presynaptic Mechanisms Involved in Neurotransmitter Release From Rat Brain." *Brain Research Protocols* 7, no. 2: 94–102. https://doi.org/10.1016/S1385-299X(00)00058-1.

Glock, C., M. Heumüller, and E. M. Schuman. 2017. "mRNA Transport & Local Translation in Neurons." *Current Opinion in Neurobiology* 45: 169–177. https://doi.org/10.1016/j.conb.2017.05.005.

Gordon, J. A., and M. P. Stryker. 1996. "Experience-Dependent Plasticity of Binocular Responses in the Primary Visual Cortex of the Mouse." *Journal of Neuroscience* 16, no. 10: 3274–3286. https://doi.org/10.1523/jneurosci.16-10-03274.1996.

Gray, E. G., and V. P. Whittaker. 1962. "The Isolation of Nerve Endings From Brain: An Electron-Microscopic Study of Cell Fragments Derived by Homogenization and Centrifugation." *Journal of Anatomy* 96, no. 1: 79–88.

Hafner, A. S., P. G. Donlin-Asp, B. Leitch, E. Herzog, and E. M. Schuman. 2019. "Local Protein Synthesis is a Ubiquitous Feature of Neuronal Pre- and Postsynaptic Compartments." *Science* 364, no. 6441: eaau3644. https://doi.org/10.1126/science.aau3644.

Halliday, M., H. Radford, K. A. M. Zents, et al. 2017. "Repurposed Drugs Targeting eIF2α-P-Mediated Translational Repression Prevent Neurodegeneration in Mice." *Brain* 140, no. 6: 1768–1783. https://doi.org/10.1093/brain/awx074.

Hoffmann, S., C. Otto, S. Kurtz, et al. 2009. "Fast Mapping of Short Sequences With Mismatches, Insertions and Deletions Using Index Structures." *PLoS Computational Biology* 5, no. 9: 1–10. https://doi.org/10.1371/journal.pcbi.1000502.

Holt, C. E., K. C. Martin, and E. M. Schuman. 2019. "Local Translation in Neurons: Visualization and Function." *Nature Structural and Molecular Biology* 26, no. 7: 557–566. https://doi.org/10.1038/s41594-019-0263-5.

Holt, C. E., and E. M. Schuman. 2013. "The Central Dogma Decentralized: New Perspectives on RNA Function and Local Translation in Neurons." *Neuron* 80, no. 3: 648–657. https://doi.org/10.1016/j.neuron.2013.10.036.

Huttlin, E. L., M. P. Jedrychowski, J. E. Elias, et al. 2010. "A Tissue-Specific Atlas of Mouse Protein Phosphorylation and Expression." *Cell* 143, no. 7: 1174–1189. https://doi.org/10.1016/j.cell.2010.12.001.

Ishimoto, T., K. Ninomiya, R. Inoue, M. Koike, Y. Uchiyama, and H. Mori. 2017. "Mice Lacking BCAS1, a Novel Myelin-Associated Protein, Display Hypomyelination, Schizophrenia-Like Abnormal Behaviors, and Upregulation of Inflammatory Genes in the Brain." *Glia* 65, no. 5: 727–739. https://doi.org/10.1002/glia.23129.

Kelmer Sacramento, E., J. M. Kirkpatrick, M. Mazzetto, et al. 2020. "Reduced Proteasome Activity in the Aging Brain Results in Ribosome Stoichiometry Loss and Aggregation." *Molecular Systems Biology* 16, no. 6: e9596. https://doi.org/10.15252/msb.20209596.

Kim, H. S., and A. M. Pickering. 2023. "Protein Translation Paradox: Implications in Translational Regulation of Aging." *Frontiers in Cell and Development Biology* 11: 1129281. https://doi.org/10.3389/fcell.2023.1129281.

Kriebel, M., J. Wuchter, S. Trinks, and H. Volkmer. 2012. "Neurofascin: A Switch Between Neuronal Plasticity and Stability." *International Journal of Biochemistry and Cell Biology* 44, no. 5: 694–697. https://doi.org/10.1016/j.biocel.2012.01.012.

Lawrence, M., R. Gentleman, and V. J. Carey. 2009. "Rtracklayer: An R Package for Interfacing With Genome Browsers." *Bioinformatics* 25, no. 14: 1841–1842. https://doi.org/10.1093/bioinformatics/btp328.

Lawrence, M., W. Huber, H. Pagès, et al. 2013. "Software for Computing and Annotating Genomic Ranges." *PLoS Computational Biology* 9, no. 8: 1–10. https://doi.org/10.1371/journal.pcbi.1003118.

Leemans, R., G. Asrar, A. Busalacchi, et al. 2009. "Developing a Common Strategy for Integrative Global Environmental Change Research and Outreach: The Earth System Science Partnership (ESSP)." *Current Opinion in Environmental Sustainability* 1, no. 1: 4–13. https://doi.org/10.1016/j.cosust.2009.07.013.

Lemaître, H., F. Crivello, B. Grassiot, A. Alpérovitch, C. Tzourio, and B. Mazoyer. 2005. "Age- and Sex-Related Effects on the Neuroanatomy of Healthy Elderly." *NeuroImage* 26, no. 3: 900–911. https://doi.org/10.1016/j.neuroimage.2005.02.042.

Lemaître, H., A. L. Goldman, F. Sambataro, et al. 2012. "Normal Age-Related Brain Morphometric Changes: Nonuniformity Across Cortical Thickness, Surface Area and Gray Matter Volume?" *Neurobiology of Aging* 33, no. 3: 1–9. https://doi.org/10.1016/j.neurobiolaging.2010.07.013.

Leventhal, A. G., Y. Wang, M. Pu, Y. Zhou, and Y. Ma. 2003. "GABA and Its Agonists Improved Visual Cortical Function in Senescent Monkeys." *Science* 300, no. 5620: 812–815. https://doi.org/10.1126/science.1082874.

Li, H., B. Handsaker, A. Wysoker, et al. 2009. "The Sequence Alignment/Map Format and SAMtools." *Bioinformatics* 25, no. 16: 2078–2079. https://doi.org/10.1093/bioinformatics/btp352.

Li, M., Z. Cui, Y. Niu, et al. 2010. "Synaptogenesis in the Developing Mouse Visual Cortex." *Brain Research Bulletin* 81, no. 1: 107–113. https://doi.org/10.1016/j.brainresbull.2009.08.028.

Li, Y. I., D. A. Knowles, J. Humphrey, et al. 2018. "Annotation-Free Quantification of RNA Splicing Using LeafCutter." *Nature Genetics* 50, no. 1: 151–158. https://doi.org/10.1038/s41588-017-0004-9.

Liao, Y., G. K. Smyth, and W. Shi. 2014. "featureCounts: An Efficient General Purpose Program for Assigning Sequence Reads to Genomic Features." *Bioinformatics* 30, no. 7: 923–930. https://doi.org/10.1093/bioinformatics/btt656.

Liao, Y., J. Wang, E. J. Jaehnig, Z. Shi, and B. Zhang. 2019. "WebGestalt 2019: Gene Set Analysis Toolkit With Revamped UIs and APIs." *Nucleic Acids Research* 47, no. W1: W199–W205. https://doi.org/10.1093/nar/gkz401.

Lopez, J., S. W. John, T. Tenev, et al. 2011. "CARD-Mediated Autoinhibition of cIAP1's E3 Ligase Activity Suppresses Cell Proliferation and Migration." *Molecular Cell* 42, no. 5: 569–583. https://doi.org/10.1016/j.molcel.2011.04.008.

Love, M. I., W. Huber, and S. Anders. 2014. "Moderated Estimation of Fold Change and Dispersion for RNA-Seq Data With DESeq2." *Genome Biology* 15, no. 12: 550. https://doi.org/10.1186/s13059-014-0550-8.

Luo, W., M. S. Friedman, K. Shedden, K. D. Hankenson, and P. J. Woolf. 2009. "GAGE: Generally Applicable Gene Set Enrichment for Pathway Analysis." *BMC Bioinformatics* 10: 161. https://doi.org/10.1186/1471-2105-10-161.

Lury, D. A. 1972. "Statistical Methods for Research Workers." *Journal of the Royal Statistical Society. Series D (The Statistician)* 21, no. 3: 229. JSTOR. https://doi.org/10.2307/2986695.

Marino, A., D. Di Fraia, D. Panfilova, et al. 2025. "Aging and Diet Alter the Protein Ubiquitylation Landscape in the Mouse Brain." *Nature Communications* 16: 5266. https://doi.org/10.1038/s41467-025-60542-6.

Moczulska, K. E., P. Pichler, M. Schutzbier, A. Schleiffer, S. Rumpel, and K. Mechtler. 2014. "Deep and Precise Quantification of the Mouse Synaptosomal Proteome Reveals Substantial Remodeling During Postnatal Maturation." *Journal of Proteome Research* 13, no. 10: 4310–4324. https://doi.org/10.1021/pr500456t.

Monday, H. R., S. C. Kharod, Y. J. Yoon, R. H. Singer, and P. E. Castillo. 2022. "Presynaptic FMRP and Local Protein Synthesis Support Structural and Functional Plasticity of Glutamatergic Axon Terminals." *Neuron* 110, no. 16: 2588–2606.e6. https://doi.org/10.1016/j.neuron.2022.05.024. Epub 2022 Jun 20.

Morrison, J. H., and P. R. Hof. 2007. "Life and Death of Neurons in the Aging Cerebral Cortex." *International Review of Neurobiology* 81: 41–57. https://doi.org/10.1016/S0074-7742(06)81004-4.

Nyberg, L., M. Lövdén, K. Riklund, U. Lindenberger, and L. Bäckman. 2012. "Memory Aging and Brain Maintenance." *Trends in Cognitive Sciences* 16, no. 5: 292–305. https://doi.org/10.1016/j.tics.2012.04.005.

Ouwenga, R., A. M. Lake, D. O'Brien, A. Mogha, A. Dani, and J. D. Dougherty. 2017. "Transcriptomic Analysis of Ribosome-Bound mRNA in Cortical Neurites In Vivo." *Journal of Neuroscience* 37, no. 36: 8688–8705. https://doi.org/10.1523/JNEUROSCI.3044-16.2017.

Pakkenberg, B., D. Pelvig, L. Marner, et al. 2003. "Aging and the Human Neocortex." *Experimental Gerontology* 38, no. 1–2: 95–99. https://doi.org/10.1016/s0531-5565(02)00151-1.

Peleg, S., F. Sananbenesi, A. Zovoilis, et al. 2010. "Altered Histone Acetylation Is Associated With Age-Dependent Memory Impairment in Mice." *Science* 328, no. 5979: 753–756. https://doi.org/10.1126/science.1186088.

Piol, D., T. Robberechts, and S. Da Cruz. 2023. "Lost in Local Translation: TDP-43 and FUS in Axonal/Neuromuscular Junction Maintenance and Dysregulation in Amyotrophic Lateral Sclerosis." *Neuron* 111, no. 9: 1355–1380. https://doi.org/10.1016/j.neuron.2023.02.028.

Raj, T., Y. I. Li, G. Wong, et al. 2018. "Integrative Transcriptome Analyses of the Aging Brain Implicate Altered Splicing in Alzheimer's Disease Susceptibility." *Nature Genetics* 50, no. 11: 1584–1592. https://doi.org/10.1038/s41588-018-0238-1.

Raz, N., U. Lindenberger, K. M. Rodrigue, et al. 2005. "Regional Brain Changes in Aging Healthy Adults: General Trends, Individual Differences and Modifiers." *Cerebral Cortex* 15, no. 11: 1676–1689. https://doi.org/10.1093/cercor/bhi044.

Richter, K. N., H. Wildhagen, M. S. Helm, J. E. Ußling, T. Schikorski, and S. O. Rizzoli. 2018. "Comparative Synaptosome Imaging: A Semi-Quantitative Method to Obtain Copy Numbers for Synaptic and Neuronal Proteins." *Scientific Reports* 8, no. 1: 14838. https://doi.org/10.1038/s41598-018-33130-6.

Robinson, J. T., H. Thorvaldsdóttir, W. Winckler, et al. 2011. "Integrative Genomics Viewer." *Nature Biotechnology* 29, no. 1: 24–26. https://doi.org/10.1038/nbt.1754.

Rybak-Wolf, A., C. Stottmeister, P. Glažar, et al. 2014. "Circular RNAs in the Mammalian Brain Are Highly Abundant, Conserved, and Dynamically Expressed." *Molecular Cell* 58, no. 5: 870–885. https://doi.org/10.1016/j.molcel.2015.03.027.

Sacramento, E. K., J. M. Kirkpatrick, M. Mazzetto, et al. 2019. "Reduced Proteasome Activity in the Aging Brain Results in Ribosome Stoichiometry Loss and Aggregation." *BioRxiv*. https://doi.org/10.1101/577478.

Salamov, A. A., T. Nishikawa, and M. B. Swindells. 1998. "Assessing Protein Coding Region Integrity in cDNA Sequencing Projects." *Bioinformatics* 14, no. 5: 384–390. https://doi.org/10.1093/bioinformatics/14.5.384.

Seo, S. S., S. R. Louros, N. Anstey, et al. 2022. "Excess Ribosomal Protein Production Unbalances Translation in a Model of Fragile X Syndrome." *Nature Communications* 13, no. 1: 3236. https://doi.org/10.1038/s41467-022-30979-0.

Sharma, K., S. Schmitt, C. Bergner, et al. 2015. "Cell Type– and Brain Region–Resolved Mouse Brain Proteome." *Nature Neuroscience* 18: 1819–1831. https://doi.org/10.1038/nn.4160.

Shigeoka, T., M. Koppers, H. H. Wong, et al. 2019. "On-Site Ribosome Remodeling by Locally Synthesized Ribosomal Proteins in Axons." *Cell Reports* 29, no. 11: 3605–3619.e10. https://doi.org/10.1016/j.celrep.2019.11.025.

Silke, J., and P. Meier. 2013. "Inhibitor of Apoptosis (IAP) Proteins-Modulators of Cell Death and Inflammation." *Cold Spring Harbor Perspectives in Biology* 5, no. 2: 1–19. https://doi.org/10.1101/cshperspect.a008730.

Smalheiser, N. R., G. Lugli, H. Zhang, H. Rizavi, E. H. Cook, and Y. Dwivedi. 2014. "Expression of microRNAs and Other Small RNAs in Prefrontal Cortex in Schizophrenia, Bipolar Disorder and Depressed Subjects." *PLoS One* 9, no. 1: 1–12. https://doi.org/10.1371/journal.pone.0086469.

Srivastava, S. 2017. "The Mitochondrial Basis of Aging and Age-Related Disorders." *Genes (Basel)* 8, no. 12: 398. https://doi.org/10.3390/genes8120398.

Sun, C., A. Nold, C. M. Fusco, et al. 2021. "The Prevalence and Specificity of Local Protein Synthesis During Neuronal Synaptic Plasticity." *Science Advances* 7, no. 38: eabj0790. https://doi.org/10.1126/sciadv.abj0790.

Suzuki, S., N. Ayukawa, C. Okada, et al. 2017. "Spatio-Temporal and Dynamic Regulation of Neurofascin Alternative Splicing in Mouse Cerebellar Neurons." *Scientific Reports* 7, no. 1: 1–13. https://doi.org/10.1038/s41598-017-11319-5.

Tao-Cheng, J. H. 2020. "Immunogold Labeling of Synaptic Vesicle Proteins in Developing Hippocampal Neurons." *Molecular Brain* 13, no. 1: 9. https://doi.org/10.1186/s13041-020-0549-x.

The Gene Ontology Consortium. 2017. "Expansion of the Gene Ontology Knowledgebase and Resources." *Nucleic Acids Research* 45, no. D1: D331–D338. https://doi.org/10.1093/nar/gkw1108. Epub 2016 Nov 29.

Thorvaldsdóttir, H., J. T. Robinson, and J. P. Mesirov. 2013. "Integrative Genomics Viewer (IGV): High-Performance Genomics Data Visualization and Exploration." *Briefings in Bioinformatics* 14, no. 2: 178–192. https://doi.org/10.1093/bib/bbs017.

Trebesova, H., and M. Grilli. 2023. "Synaptosomes: A Functional Tool for Studying Neuroinflammation." *Encyclopedia* 3, no. 2: 406–418. https://doi.org/10.3390/encyclopedia3020027.

von Kügelgen, N., and M. Chekulaeva. 2020. "Conservation of a Core Neurite Transcriptome Across Neuronal Types and Species." *Wiley Interdisciplinary Reviews: RNA* 11, no. 4: e1590. https://doi.org/10.1002/wrna.1590.

Wang, M., N. J. Gamo, Y. Yang, et al. 2011. "Neuronal Basis of Age-Related Working Memory Decline." *Nature* 476, no. 7359: 210–213. https://doi.org/10.1038/nature10243.

Watson, E. T., M. M. Pauers, M. J. Seibert, J. D. Vevea, and E. R. Chapman. 2023. "Synaptic Vesicle Proteins are Selectively Delivered to Axons in Mammalian Neurons." *eLife* 12: e82568. https://doi.org/10.7554/eLife.82568.

Wei, Y. N., H. Y. Hu, G. C. Xie, et al. 2015. "Transcript and Protein Expression Decoupling Reveals RNA Binding Proteins and miRNAs as Potential Modulators of Human Aging." *Genome Biology* 16, no. 1: 41. https://doi.org/10.1186/s13059-015-0608-2.

Yin, T., D. Cook, and M. Lawrence. 2012. "Ggbio: An R Package for Extending the Grammar of Graphics for Genomic Data." *Genome Biology* 13, no. 8: 1–14. https://doi.org/10.1186/gb-2012-13-8-r77.

You, X., I. Vlatkovic, A. Babic, et al. 2015. "Neural Circular RNAs Are Derived From Synaptic Genes and Regulated by Development and Plasticity." *Nature Neuroscience* 18, no. 4: 603–610. https://doi.org/10.1038/nn.3975.

Yu, Q., H. Xiao, M. P. Jedrychowski, et al. 2020. "Sample Multiplexing for Targeted Pathway Proteomics in Aging Mice." *Proceedings of the National Academy of Sciences of the United States of America* 117, no. 18: 9723–9732. https://doi.org/10.1073/pnas.1919410117. Epub 2020 Apr 24.

Zappulo, A., D. Van Den Bruck, C. Ciolli Mattioli, et al. 2017. "RNA Localization Is a Key Determinant of Neurite-Enriched Proteome." *Nature Communications* 8, no. 1: 583. https://doi.org/10.1038/s41467-017-00690-6.

Supporting Information

Additional supporting information can be found online in the Supporting Information section. **Figure S1:** acel70262-sup-0001-FigureS1.pdf. **Figure S2:** acel70262-sup-0002-FigureS2.pdf. **Figure S3:** acel70262-sup-0003-FigureS3.pdf. **Figure S4:** acel70262-sup-0004-FigureS4.pdf. **Figure S5:** acel70262-sup-0005-FigureS5.pdf. **Figure S6:** acel70262-sup-0006-FigureS6.pdf. **Figure S7:** acel70262-sup-0007-FigureS7.pdf. **Figure S8:** acel70262-sup-0008-FigureS8.pdf. **Figure S9:** acel70262-sup-0009-FigureS9.pdf. **Figure S10:** acel70262-sup-0010-FigureS10.pdf. **Figure S11:** acel70262-sup-0011-FigureS11.pdf. **Figure S12:** acel70262-sup-0012-FigureS12.pdf. **Figure S13:** acel70262-sup-0013-FigureS13.pdf. **Figure S14:** acel70262-sup-0014-FigureS14.pdf. **Table S1–S4:** acel70262-sup-0014-TableS1–S4.docx.